Investigating the Impact of Small Intestine Architecture on Nutrient Absorption *in vitro*

An Honors Thesis for the Department of Biomedical Engineering

Megan R. Houchin

Tufts University, 2023

Acknowledgments

The completion of this study would not have been possible without the expertise, advice, and constant support of my thesis committee members, Dr. David Kaplan and Dr. Ying Chen. I owe you both a debt of gratitude for guiding me since my sophomore year and allowing me the opportunity to find my voice and passion within research.

A special thanks to Sara Rudolph and Brooke Longo for their collaboration, mentorship, and advice throughout this project and my undergraduate education. Additional thanks to Schlomit David and Edward Gordon for providing feedback and encouragement throughout the year. Thanks to Olivia Foster, Brooke Wang, Udathari Kumarasinghe, Malak Oufessa, Fatimah Mumuney, and Mina Shokoufandeh for your support and consultation throughout the thesis process.

I would also like to thank my parents, Michele Laine and John Houchin. Without you, this project would not have been possible. Finally, thank you to my friends Jacob Newmark, Duru Ugurlu, Becca Gomez, and Robert Kaplan and my dogs, Layla and Bushi, your belief in me and your emotional support kept my spirits high throughout this process.

Table of Contents

List of Tables

List of Figures

Abstract

The architecture of the small intestine is a direct determinant of nutritional absorption efficiency. The curvature of the luminal walls and the presence of villus structures are crucial features for maintaining gut homeostasis. To model nutritional absorption in the intestine, three-dimensional (3D) printing and inverse molding techniques were utilized to form 3D, spongy, silk fibroin scaffold systems that resemble the cylindrical structure and villus microarchitecture. Five scaffold designs were created to isolate or combine the distinct features of the small intestine's architecture. The key features of the small intestine that were compared included the curvature of the lumen and the structure of the villi. Intestinal cell (Caco-2, HT29-MTX) attachment, growth, and *in vitro* culture support were demonstrated in the scaffolds. Iron was selected as a model nutrient to study nutritional absorption efficiency due to its crucial role in growth and development for almost all living organisms. Although iron is widely available in food and supplements, iron deficiency remains one of the most common nutritional deficiencies, making it an important area of research. The formation of ferritin, the intracellular iron storage protein, was used to measure iron absorption as ferritin is upregulated in response to iron uptake. Ferritin levels from each scaffold type were quantified using an enzyme-linked immunoassay (ELISA) and visualized through immunostaining. Our findings suggest the villus structures in the small intestine are the primary determinant of iron absorption, while the curvature of the lumen has a less significant impact. This study established a novel *in vitro* intestinal epithelial model for investigating iron absorption within

the small intestine, without the ethical and practical limitations of animal and human studies.

Introduction

The Small Intestine's Function and Architecture

About 90% of nutritional absorption occurs in the small intestine. [1] As nutrients flow through the small intestine, specialized cells lining the walls of the organ absorb the nutrients, producing energy to sustain the body's homeostasis. [2] The small intestine measures approximately 22 feet in length in adults, resembling a long, narrow tube. [3] Attached to the luminal wall of the small intestine exist thousands of finger-like protrusions, known as villi. [4] These villi range from 0.2 to 1 mm in length and 100 to 200 μm in diameter and vary in size from tip to base. [4] Each villus is surrounded by small invaginations known as crypts. [5] These crypts can range from 100 to 200 μm in length and 50 to 150 μm in diameter. [6] This crypt-villus architecture plays a vital role in maintaining intestinal homeostasis and promoting renewal. [6] Highly proliferative stem cell populations are present within the crypts. [5] Along the crypt-villus axis, intestinal stem cells residing in the crypts give rise to differentiated epithelial cells, which then migrate up and eventually cover the villi projections. The mature intestinal epithelium consists of four major populations of cells: enterocytes, goblet cells, enteroendocrine cells, and Paneth cells. [6] The coordinated interactions between these cells are crucial for maintaining the intestinal barrier, regulating nutrient absorption, and protecting the gut from harmful microorganisms. Intestinal epithelial cells have a high turnover rate and are replaced every 5-7 days. As cells reach the tip of the villi,

they die and are shed, while new, differentiated cells migrate upward to replace the diminished epithelial barrier. This process results in the continuous renewal of cells, ensuring the proper functioning of the small intestine. [5,7] The structures within the small intestine also significantly increase gut surface area to maximize nutrient absorption, which is essential for maintaining optimal health of the digestive system. [8] However, abnormal crypt-villus structures have been linked to intestinal dysfunctions and disorders such as celiac disease (CD), inflammatory bowel disease (IBD), and intestinal cancer as revealed by previous studies. [9] Given that crypts play a primary role in cell differentiation and development, the present study explores how the curvature of the luminal walls and villus structures influence nutritional absorption.

Development of an in vitro Small Intestine Model

Several advances have been made to develop a 3D *in vitro* model of the small intestine. Often, 2D monolayers of organoids, Caco-2, and other intestinal cell lines have been used to model small intestinal behavior and environment. [10] 2D cell culturing often has been utilized because organoid-derived epithelial cells and other intestinal cell lines can be accessed easily when seeded in a 2D monolayer, supporting studies involving drug absorption, nutrient absorption, microbe interactions, or the inclusion of relevant cell types such as stromal or immune cells. [5, 11] However, these models have many limitations such as an inability to recreate the 3D intestinal lumen and relevant architectures, the inclusion of biochemical gradients, and dynamic mechanical forces, which are all

critical for cell differentiation and behavior. [5, 11] A 3D *in vitro* model provides an alternative that ensures a complete representation of cell-cell and cell-matric interactions. [11]

In response to the demand for small intestine 3D culture systems, recent studies have extensively explored developing this area of study. [12] These studies have aimed at reproducing a more accurate human intestine 3D architecture and biochemical gradient. [12] In a recent study, poly(lactic-co-glycolic acid) scaffolds with a porous architecture and villi were seeded with Caco-2 and HT29-MTX cells. [13] These scaffolds were designed using 3D printing technology. By introducing villus structures, epithelial cells exhibited differentiation with response to biochemical microenvironments of the intestine using both apical and basolateral feeding. [13] Additionally, another study created micro-molded cross-linked collagen and organoid-derived intestinal epithelial cells to reproduce mature villus and crypt-like architecture. [6] Alternatively, our lab was able to combine silk fibroin and collagen type I to generate a system that is mechanically stable, cytocompatible, and versatile in morphology and structure to support intestinal features. [5] Silk was chosen as a key biomaterial because it is a widely used biocompatible, natural polymer with tunable mechanical properties. [5] The study designed scaffolds with crypt and villi architecture within a curved luminal surface using CAD software and 3D printed these designs. Using these designs, the study used inverse-molding techniques and then froze, lyophilized, and cross-linked the silk into sponges that provided a porous structure. [5] To provide further support, collagen type I solution was added to the sponges to provide support for

cell attachment, proliferation, and differentiation. [5] All these studies demonstrated the importance of 3D topology in promoting cell polarization, differentiation, and nutrient absorption; however, the last mentioned accomplished this task the best. [5] The current study utilized this methodology to produce variations of the described silk scaffolds to isolate and combine features of the small intestinal architecture because the method can accomplish customizing 3D biomimetic scaffolds with a high degree of complexity and precision that can support multiple cell types.

Furthermore, as above mentioned, several epithelial cell types cover the crypt-villus axis *in vivo* including enterocytes, goblet cells, enteroendocrine cells, and Paneth cells. [5] Enterocytes are the specialized cells primarily responsible for the absorption of nutrients from digested food. [14] They have microvilli on their surface, greatly increasing their surface area for absorption. [14] Enterocytes also contain various transport proteins and channels in their cell membranes that allow for the movement of nutrients from the lumen of the small intestine into the bloodstream. [14] Additionally, enterocytes produce various enzymes and hormones that aid in the digestion and absorption of nutrients. [14] In the current study the cells that were used were Caco-2 and HT29-MTX cells. Caco-2 cells are originally derived from colon carcinoma. [15] Caco-2 cells, however, are often used in *in vitro* small intestine modeling because they differentiate into a monolayer of cells that have many properties typical of absorptive enterocytes with brush border layer characteristics as found in the small intestine. [15] Thus, Caco-2 cells were included in this study. [5, 15] HT29-MTX cells were also included in the co-culture. The HT29-MTX cell line, derived from human colorectal

adenocarcinoma and exhibiting an epithelial morphology, can be induced to differentiate into mature goblet cells capable of producing mucus through treatment with methotrexate. These cells are particularly valuable for investigating the mucus barrier of the gastrointestinal tract and its interactions with nutrients, drugs, and pathogens. [16] Throughout the gastrointestinal tract, goblet cells secrete sticky mucus, creating a mucosa layer. [16] On this layer, villi project increasing surface area for nutritional absorption. [16] The mucus also lubricates food masses to facilitate movement and forms a protective layer over the epithelial lining. [16] Additionally, Caco-2 and HT29-MTX cells were chosen for the present study due to their ability to thrive in this 3D environment. While organoids offer physiological relevance and cell heterogeneity, their low and inconsistent survival rate in a 3D environment makes them unreliable for this study. [5]

Iron Absorption Modeling of the Small Intestine

Iron was chosen to be the nutrient analyzed in this study for a variety of reasons. Iron deficiency is one of the most prevalent nutritional deficiencies, affecting up to 2 billion people worldwide. [17] Iron deficiency is significant because iron is a mineral essential to one's diet and naturally present in a variety of foods, added to some food products, and often ingested in dietary supplements. [18] Iron is required for numerous physiological processes, including physical growth, neurological development, and cellular function. Iron also plays a critical role in the synthesis of hormones, such as T3 and T4, which are involved in the

creation and metabolism of blood cells. [19] Furthermore, iron is an essential component of hemoglobin, an erythrocyte protein that transfers oxygen from the lungs to tissues, and myoglobin, which supports muscle development and healthy connective tissue. [18]

The Caco-2 human epithelial cell line has been widely used as a model of the intestinal epithelial barrier and is well-established as an *in vitro* model for iron absorption, used to assess the bioaccessibility of iron from foods and diets. [10] For example, one study used Caco-2 cells to compare the difference in iron bioavailability in Young Child Formulae and prebiotics with ascorbic acid to better develop a baby formula for children with iron deficiency. [20] Another study used Caco-2 cells to compare the iron bioavailability in mixtures of fresh and/or cooked foods subjected to simulated gastrointestinal digestion. [21]

On this topic, it is important to establish the iron absorption mechanism within the small intestine. [22,23,24] Many studies have shown that ascorbic acid enhances food iron availability. For iron to be absorbed in the small intestine, it must be in its oxidized state of Fe^{2+}. [23] If one were to ingest elemental iron, the iron would react with stomach acid to form Fe^{2+}. [23] Additionally, ascorbic acid enhances the bioavailability of Fe^{2+} by preventing it from oxidizing to Fe^{3+}. [23] In the upper small intestine, Fe^{2+} is more soluble due to the pH and more bioavailable than Fe^{3+}. [23] One study examined different ratios of ascorbic acid to Fe^{2+} to prevent oxidation from occurring, and found that molar ratios of at least 1.6:1 produce the highest bioavailability of iron. [23] Another study started with ferric chloride and used ascorbic acid to produce ferrous iron and increase the

bioavailability when exposed to Caco-2 cells. [21] They chose to use a 1:20 ratio of Fe^{2+} to ascorbic acid and found that it increased iron bioavailability. [21]

When enterocytes absorb iron, ferritin, a protein that stores iron inside the cells, is produced. [25] Previous studies have demonstrated that the formation of ferritin occurs in response to iron uptake and provides a measure of cell iron uptake. [25] All these previous studies used ferritin to quantify iron absorption in Caco-2 cells by either using an enzyme-linked immunoassay (ELISA) or a radioimmunoassay. One study monitored ferritin production in Caco-2 cells after exposure to iron and saw that the value plateaued after 24 hours. [21] Another study explained that after 3 hours of incubating with media mixtures of 80 and 120 μM of iron, the media of the cells was refreshed with no iron added media, and then the cell ferritin levels were tested after a total of 24 hours. [22] A third study used food samples and measured ferritin in Caco-2 cells using a FER-Iron II ferritin Assay and total iron content in samples with an inductively coupled plasma emission spectrometer. [26] It is important to note all previous studies mentioned concerning iron absorption have been with Caco-2 cell monocultures and all in 2D cultures.

The aim of this study is to investigate how the 3D luminal and villus structures of a small intestine in vitro model with varying architectures impact the absorption of iron, thereby providing insights into how organ structures affect the absorptive functions of the human gut. To establish an in vitro 3D intestinal epithelial model with varying architecture and villus structures, we incorporated two commonly used intestinal epithelial cell lines, Caco2 and HT29-MTX, into

3D silk scaffolds. The resulting model was subsequently characterized to investigate iron absorption. For the iron absorption study, 150 μM of iron was used with ascorbic acid at a 20:1 molar ratio of ascorbic acid to iron. After 24 hours, ferritin levels from each scaffold type were measured using an enzyme-linked immunoassay (ELISA) and visualized through confocal immunostaining.

Materials and Methods

Silk Processing for Scaffold Fabrication

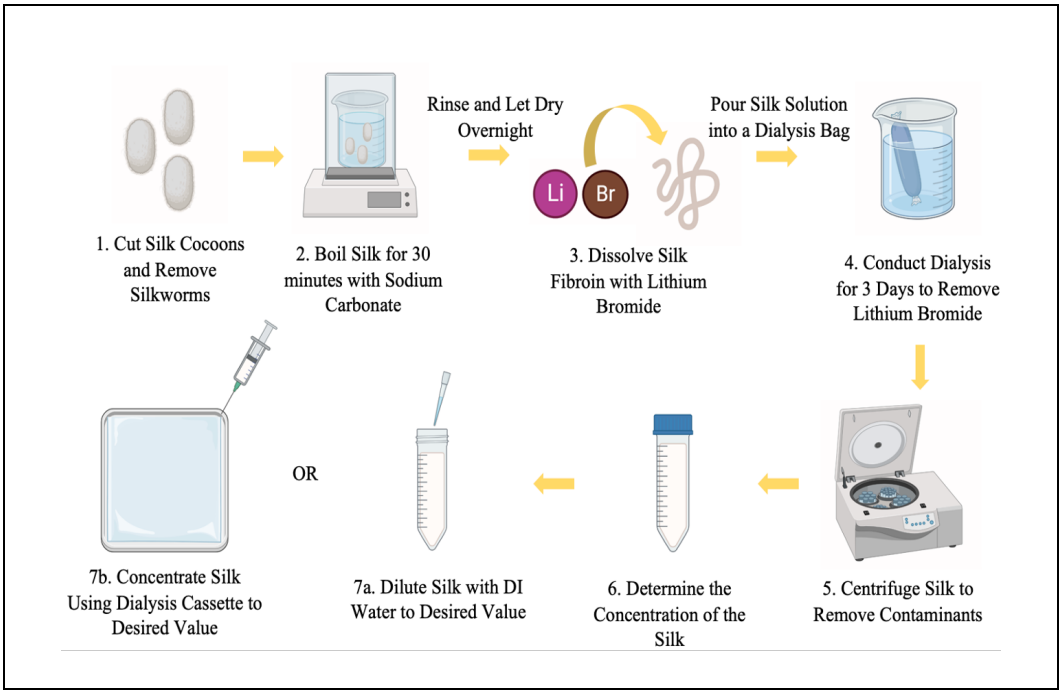

Figure 1: Overall Silk Process Summary. (1) The silk process starts by first cutting up the silk cocoons and removing the silkworms. (2) The silk was then boiled in sodium carbonate for 30 minutes, removed and rinsed for 40 minutes, then left to dry overnight. (3) The silk fibroin was then dissolved using lithium bromide and incubated at 60°C for 30 minutes, producing a silk solution. The solution was then poured into a dialysis bag and sealed. (4) The dialysis bag was placed into a 5 L beaker of distilled water and dialysis was conducted for 3 days to remove the lithium bromide. The water was changed a total of 9-10x. (5) The silk was then centrifuged at 9000 RPM for 40 minutes at 4°C to remove contaminants (silkworm residue). (6) The concentration of the silk was then determined by measuring the mass of a sample of the silk, then measuring it again after incubating it at 60°C overnight. The concentration of silk was the mass after

the incubation divided by the mass before the incubation times 100. After determining the concentration, the silk was either (7a) diluted with deionized water to the desired value or (7b) concentrated using a dialysis cassette to the desired value.

The silk solutions were prepared as previously described. [27] The overall silk process is illustrated in Figure 1. The total number of scaffolds used throughout the experiment was 140. To make one curved scaffold and one flat scaffold, one needs about 600 μL of silk and 1 mL of silk respectively. For processing a single batch of silk, 10 grams of silk cocoons (Tajima Sho Co., LTD., Yokohama, Japan), one would end up with about 90 mL of silk between 5-8% concentrated. For this experiment, the silk was concentrated to 6.5% and 7% solutions for use. All silk that was processed was used within a month of processing. To maintain the quality and freshness of the silk, we stored it at a temperature of 4°C until it was ready to be used.

Fabrication of 3D Silk Scaffolds with Varying Architecture

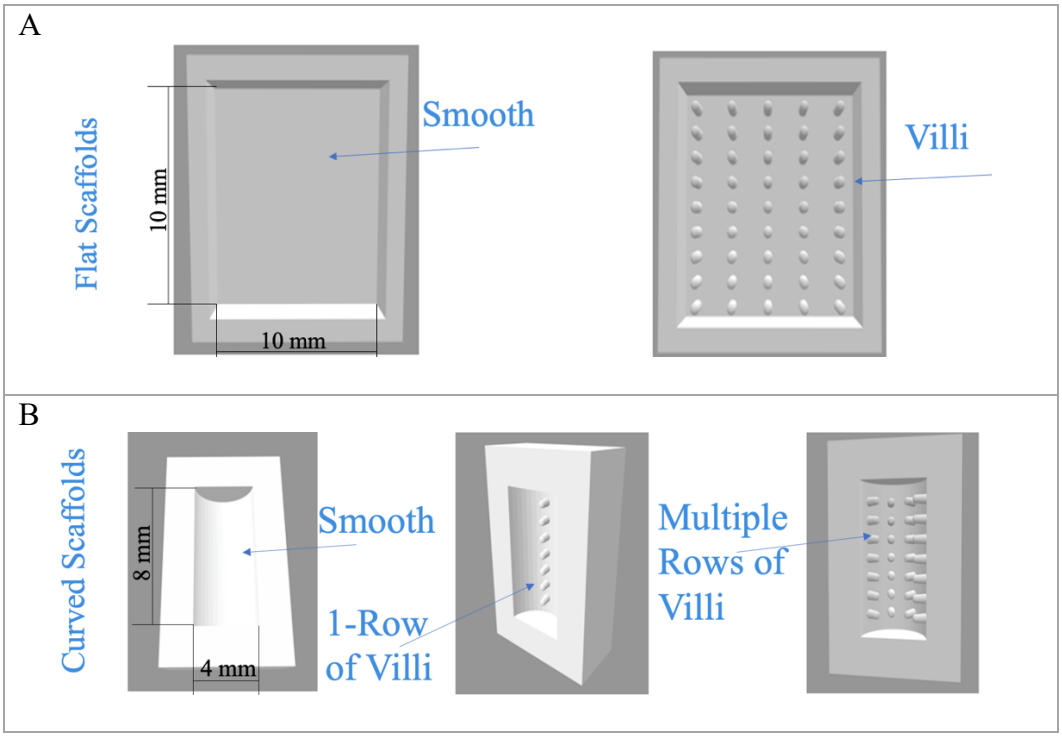

Figure 2. Architectures of each scaffold used to isolate and combine features of the small intestine. 3D half-scaffolds were designed in Solidworks and their designs are shown here. (A) The left scaffold represents the control group, being flat and without villi, while the right scaffold solely tests the effect of villi on nutritional absorption. (B) These scaffolds all model the curvature of the luminal wall. The left scaffold was used to examine the effect of curvature on nutritional absorption. The middle scaffold combines villi and curvature features, with one row of villi down the middle. The right scaffold expands on the examination of the effect of villi and curvature, by not only having more rows of villi but also thereby having the most surface area of the curved half-scaffolds.

The design and architecture of each scaffold are shown in Figure 2. The scaffolds were designed using the computer-aided design (CAD) software Solidworks, as described previously. [28] For this study, five designs were created to either isolate or combine features of the small intestine's architecture. The main features of the small intestine compared in this study are the curvature of the lumen and villi structures.

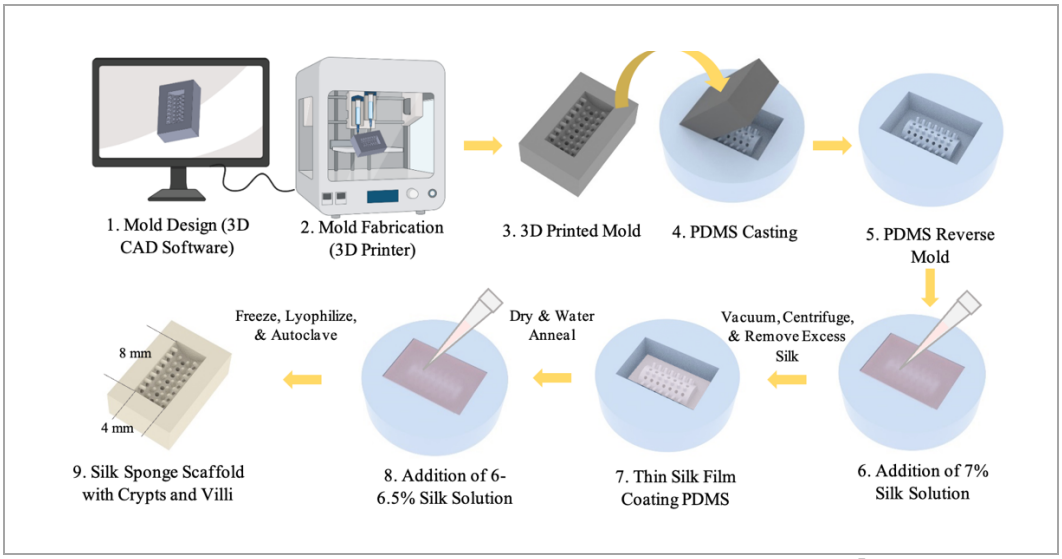

Figure 3. The overall fabrication process of silk half-scaffolds. [5] 3D half-scaffolds displaying varying features of the small intestine were fabricated by using 3D printing techniques and silk fibroin. The above visualizes how one of the types of the half-scaffolds was made, this one being curved with multiple rows of villi. The fabrication process is as follows: (1) design the 3D models using CAD software, (2-3) 3D print the resin molds, (4-5) create PDMS reverse molds with resin molds by casting the resin molds in liquid PDMS and curing the system with heat exposure, (6) pipette 7% silk into the reverse molds to cover the luminal surface, vacuum and centrifuge the filled reverse molds, remove the excess silk from the reverse molds leaving a thin silk film, and let to dry overnight, (7) water anneal the dry reverse molds, then add 6-6.5% silk filling the bulk space of the reverse molds, (8) freeze overnight, move filled reverse molds to the lyophilizer for freeze-drying for two days, and then autoclave the filled reverse molds, (9) finally, submerge the filled reverse molds in distilled water and carefully remove the spongey, silk scaffold.

The silk scaffold fabrication steps are demonstrated in Figure 3. The scaffold designs (or mold designs) were then printed using a Formlabs Form 2 resin 3D printer (Somerville, MA). After printing, the resin designs were washed for 10 minutes using the Form Wash (Somerville, MA) and cured at 60°C for 15 minutes in the Form Cure (Somerville, MA). To create the silk scaffolds, the printed resin designs were used to generate reverse molds made of polydimethylsiloxane (PDMS) (Sylgard 184 PDMS, Dow Corning, Midland, MI). After pouring the PDMS onto the resin designs in 6-well plates, they were cured

at 60°C for 2 hours. The resin designs were then carefully removed from the PDMS, making sure to not cause damage to the luminal surface and producing the reverse molds. [28] Finally, the reverse molds were washed to be prepared for silk casting.

The 3D half-scaffolds were similarly prepared as previously described. [5] To create a thin film on the surface of the PDMS reverse molds, 7% silk was used to fill the PDMS reverse molds, ensuring all the luminal surface was covered. The PDMS reverse molds were then placed in a vacuum at -25 kPa for 15 minutes. After this, the reverse molds were then centrifuged at 4°C for 5 minutes at 800*g* and the excess silk was removed, leaving a thin film on the surface of the PDMS reverse molds. The molds were then left to dry overnight in a fume hood. Next, the reverse molds were placed into a water annealer with a vacuum chamber and pumped to -25 kPa for 2 hours at 60°C. Once the films were annealed, the PDMS reverse molds were filled with 6-6.5% silk solution, filling the bulk space entirely. Immediately after filling, the molds with silk solution froze overnight at -20°C. The next day, the filled PDMS molds were quickly moved into the lyophilizer to freeze-dry over the course of two days. After freeze-drying, the filled molds were autoclaved, inducing β-sheet formation. To then remove the spongy, silk scaffolds from the PDMS reverse molds without damaging the luminal surfaces, the filled molds were submerged and soaked in deionized water for 24 hours.

After allowing the removed scaffolds to dry, they were trimmed into a rectangle. The dimensions and features of each type of scaffold can be seen in Table 1. The fabrication process produced different variations of half-scaffolds,

some with patterned villus structure units and others with plain smooth lumens, but all had a porous bulk space.

Scaffold Type:	Length (mm):	Width (mm):	Height (mm):	Surface Area (mm^2):	Number of Villi:
Flat, no Villi	10	10	2	100.00	0
Flat, w/ Villi	10	10	2	165.35	45
Curved, no Villi	4	8	2	50.24	0
Curved, one row of Villi	4	8	2	60.41	7
Curved, multiple rows of Villi	4	8	2	90.90	28

Table 1. Dimensions and features of silk half-scaffolds. The features examined in this study are surface area, villi structures being present in the lumen, and the curved nature of the small intestine. These features are isolated and combined in the scaffold designs described in the table to see their effect on the nutritional absorption of iron.

Caco-2 and HT29 Cell Source and Maintenance in 2D Flask System

Caco-2 (ATCC; Rockville, MD) and HT29-MTX (HT29) (Public Health England Culture Collection; Salisbury, Great Britain) intestinal epithelial cell lines were first plated on T175 cell culture flasks (ThermoFisher Scientific) and allowed to mature for 2 weeks prior to cell seeding on 3D silk scaffolds. During this time, they were passaged when 90-100% confluent and fed every other day with DMEM with GlutaMAX supplement (ThermoFisher Scientific)

supplemented with 10% fetal bovine serum (FBS) (ThermoFisher Scientific), 10 μg/mL human transferrin (Gibco, Gaithersburg, MD), and 6 mL of Penicillin-Streptomycin (ThermoFisher Scientific). The cells were allowed to grow until the necessary amounts were attained for seeding at a 3:1 ratio of Caco-2 to HT29 cells and a cell density of 2 x 10^6 cells/mL on each scaffold. [5] For the entire study, Caco-2 cells from passage numbers 24-28 and HT29 cells from passage numbers 43-48 were used for seedings.

Cell Seeding and Culture

As stated previously, the cells were seeded on the scaffolds at a 3:1 ratio of Caco-2 to HT29 cells at a density of 2 x 10^6 cells/mL. The following was done for every cell seeding that occurred throughout this study. Prior to seeding the cells on the scaffolds, a collagen solution was first prepared with collagen, 10x DMEM, media as described above, and sodium hydroxide, NaOH. [28] The pH of the collagen solution was between 7.4-7.8, determined based on the color of the solution containing phenol red. This collagen mixture was then added to cover both sides of the scaffolds (top and bottom), thereby filling in any holes in the silk film and preventing cells from falling through. [28] The curved scaffolds were moved into 24-well plates while the flat scaffolds were moved into 12-well plates. The lumens of the 3D half-scaffolds were seeded with cells and left in the incubator for 10 minutes with 50 μL of media as described above on the curved scaffolds and 300 μL of media on the flat scaffolds. [5] Then, an additional 300 μL of media was added to the bottom of each well for the curved scaffolds, and 500

μL was added for the flat scaffolds, to prevent them from drying out. After then incubating for another 30 minutes, allowing for cell attachment, 700 μL and 1000 μL of media were added to each of the curved scaffolds' and flat scaffolds' wells respectively, to maintain a suitable microenvironment for cell growth. The curved and flat scaffolds were fed every other day with 1 mL and 1.5 mL of media, respectively for two weeks of culture. After one week of culturing, the scaffolds were moved to new well plates to ensure no cells were growing on the bottom of the plates.

Immunofluorescence and Confocal Imaging of Scaffolds

To ensure cells were differentiated sufficiently during the time of iron introduction, cells were seeded on all five types of scaffolds to analyze differentiation and cell representation two weeks after initial seedings. Conducting immunofluorescent staining and imaging on half-scaffolds has been previously described. [28] After two weeks of culturing, seeded silk scaffolds were fixed with paraformaldehyde (PFA), then the cells were penetrated with triton 100 detergent, and finally, 3% bovine serum albumin (BSA) was applied to the scaffolds to prevent autofluorescence of the silk. After permeabilization and blocking, antibodies were added to the scaffolds' luminal surfaces. Anti-human ZO-1 conjugated with Alexa Fluor 594 Conjugate (Thermofisher, 1:100) was used and then incubated at 4 °C for two nights prior to imaging. Primary antibodies used were anti-human-MUC-2 (Santa Cruz Biotech, 1:50) and anti-sucrase isomaltase (SI) (Santa Cruz Biotech, 1:50) and then removed the

following day. The scaffolds were then stained with Alexa Fluor 594 goat-anti-mouse secondary antibody at 1:250 (Invitrogen) and Alexa Fluor 488 goat-anti-rabbit secondary antibody at 1:250 (Invitrogen). The scaffolds were then counterstained with dihydrochloride (DAPI, Invitrogen) for nuclei and then let to incubate overnight at 4°C.

Before confocal imaging, the scaffolds were trimmed to better expose the luminal surfaces. The luminal surfaces were observed and imaged using a Leica SP confocal microscope. The filters used were for DAPI (Ex/Em: 350/470 nm), Texas Red (Ex/Em: 540/605 nm), and GFP/FITC (Ex/Em: 488/514 nm). To create the 3D rendered images, Leica confocal software (application site X, 3.3.0.16799 and ImageJ) was used.

Scanning Electron Microscopy (SEM) of 3D Silk Scaffolds

Conducting SEM on half-scaffolds has been previously described. [5] The unseeded scaffolds were dehydrated by submerging and incubating them in increasing concentrations of ethanol solution every hour. The concentrations of ethanol used were 30%, 50%, 70%, 90%, and 100% twice, before finally submerging the samples in hexamethyldisilazane (HMDS) to reach critical point drying overnight in a chemical hood (Somerville, MA). Critical drying point occurs at the temperature and pressure that results in zero surface tension. This is achieved so that biological specimens avoid damage to their surfaces to be visualized. During the 30% and 50% ethanol incubations, the samples were kept at 4°C, and during the remaining incubations, the samples were kept at -20°C.

After dehydration, the samples were trimmed so only the luminal surfaces were exposed and then mounted on metal stubs. The samples were then sputter-coated with 10 nm of Pt/Pd with a sputter coater (209HR, Cressington Scientific Instruments, Inc.). Finally, the samples were imaged on a scanning electron microscope (SEM) (Zeiss UltraPlus SEM, Carl Zeiss SMT, Inc.).

Iron Preparation and Feeding

Preparing iron to be fed to Caco-2 cells in a 24-well plate has been previously described. [22,23] The objective was to prepare ferrous ascorbate, $C_{12}H_{14}FeO_{12}$, solutions in diluted media. Initially, to determine whether the levels of iron would be detectable with the Human Ferritin ELISA Kit (Invitrogen), iron was introduced to Caco-2 cells in a 24-well plate and the assay was run to measure ferritin levels. The concentrations of iron observed were 120 μM and 150 μM. [22] After determining the optimal amount of iron to introduce, cells were co-cultured on all five types of scaffolds and 48-well plates so that 150 μM of iron could be introduced after 2 and 3 weeks of co-culturing.

The following iron preparation was conducted for both experiments previously described. First, a stock solution of ferric chloride, $FeCl_3$, (Sigma-Aldrich, Millipore Sigma) was created by adding 3.89 g of ferric chloride to 50 mL of UltraPure™ DNase/RNase-Free Distilled Water (ThermoFisher Scientific) creating a 480 mM ferric chloride solution. Then, 62.5 μL of the stock solution was diluted with 50 mL of the distilled water to create a 600 μM ferric chloride solution. Additionally, 78.13 μL of the 480 mM ferric chloride solution was

diluted with 49.2 mL of the distilled water to create a 750 μM ferric chloride solution.

Next, a stock solution of ascorbic acid, $C_6H_8O_6$, was created. Ascorbic acid was used because it reduces ferric chloride to ferrous ascorbate, which can then be absorbed by Caco-2 cells. [23] A 1:20 ratio of iron to ascorbic acid would accomplish this reaction. [21] 1 g of sodium ascorbate, $C_6H_7NaO_6$ (Sigma-Aldrich, Millipore Sigma), was added to 50 mL of the distilled water to create a 0.1 M ascorbic acid solution. Next, 6 mL of the 0.1 M solution was diluted in 44 mL of the distilled water to create a 12,000 μM stock solution. Additionally, 7.5 mL of the 0.1 M ascorbic acid solution was diluted in 42.5 mL of the distilled water to create a 15,000 μM stock solution.

For the 9 wells of Caco-2 cells in a 24-well plate, 30 mL of media with 120 μM of ferrous ascorbate and 30 mL of media with 150 μM of ferrous ascorbate were created. Therefore, 6 mL of the 600 μM ferric chloride solution and 6 mL of the 12,000 μM ascorbic acid solution were added to 18 mL of media to create a solution of media with 120 μM of ferrous ascorbate. Additionally, 6 mL of the 750 μM ferric chloride solution and 6 mL of the 15,000 μM ascorbic acid solution were added to 18 mL of media to create a solution of media with 150 μM of ferrous ascorbate.

Once the wells of Caco-2 cells were 80-100% confluent, three wells were fed media, three wells were fed media with 120 μM of ferrous iron, and three wells were fed media with 150 μM of ferrous iron. This was done by aspirating the media from each well and filling them with 1.5 mL of the previously indicated

solution. The cells were then incubated for 3 hours and then the media was saved by freezing the samples at -80°C for approximately a month and a half. [22] After removing the remainder of the solution from each well and washing the wells with DPBS (ThemroFisher Scientific) 2-3 times, regularly prepared media was added to each well and incubated for 24 hours. After 24 hours, more media was saved and frozen under the same conditions as previously stated and the cells were prepared for extraction as stated in the next section.

For the cells seeded on scaffolds, after 2 and 3 weeks of culturing, media with 150 μM of ferrous iron (prepared as previously described) was added to each well, giving the curved scaffolds 1 mL of media and the flat scaffolds 1.5 mL of media each. The cells were then incubated for 3 hours, then the media was discarded, and the cells were washed with DPBS 2-3 times. Regularly prepared media was then added to the wells and the cells were incubated for 24 hours. The cells were then extracted or stained.

ELISA Cell Sample Preparation

The samples were prepared using the Abcam "ELISA sample preparation guide." The well plates were placed on ice as the cells were washed with ice-cold DPBS (ThermoFisher Scientific). Prior to each use, phenylmethylsulphonyl fluoride (PMSF) protease inhibitor (ThermoFisher Scientific) was added to the cell lysis buffer. After washing, 320 μL of cell lysis buffer (ThermoFisher Scientific) was added to each well of the 2D cultures, and the cells were lysed for 30 minutes, vortexing the samples every 10 minutes. The scaffolds were then cut

up and 320 μL of cell lysis buffer was added to each well of the 3D cultures with half-scaffolds, and the cells were lysed for 30 minutes, vortexing the samples every 10 minutes. For both types of cultures, the cells were then scraped and collected in pre-chilled tubes. The tubes were then centrifuged at 13,000 rpm for 10 minutes at 4°C to pellet insoluble contents. Finally, the supernatant was aliquoted into clean, chilled tubes on ice and the samples were stored at -80°C.

Human Ferritin Assay

After collecting the samples, a ferritin assay was conducted using the Human Ferritin ELISA Kit (Invitrogen). For experimental optimization, initially, Caco-2 cells were seeded in a 24-well plate at a density of 2 x 10^6 cells/mL and allowed to culture for 8 days, as previously described. The cells were then conditioned with 0, 120, and 150 μM of ferrous ascorbate. Three samples from each of the following conditions were analyzed: media from 3 hours after incubating with specified iron conditions, media from 24 hours after incubating with specified iron conditions, and cell lysate from specified iron conditions. After analyzing that data, the ELISA was conducted on cell lysates from each of the five different scaffolds, 2D cell co-culture controls, and media controls. All samples had 150 μM of ferrous ascorbate introduced to them and the previously described feeding and cell preparation procedures were followed. These conditions were tested at weeks 2 and 3 after initial cell seedings.

A standard curve was initially conducted during the Caco-2 2D culture sample analysis and used to generate all the following results. Initial cell lysate

samples were diluted 1:1 with provided Assay Diluent B while initial media samples were not diluted. The second ELISA conducted diluted cell lysate samples 1:2 and two media conditions' samples were diluted 1:1 while the other two media conditions' samples had no dilution (as specified in the results). Absorbances were read at 450 nm and 570 nm. The absorbances read at 570 nm were subtracted from the absorbances read at 450 nm to remove background noise. Prism was used to generate the standard curve and calculate ferritin values for each condition. XLMiner Analysis ToolPak was used to conduct single-way ANOVA, which determined the p-values discussed in the results.

For samples from scaffolds cultured for 2 and 3 weeks, cell lysates were diluted 1:2 with provided Assay Diluent B. Another ELISA was conducted that diluted the cell lysate samples from the 2D well plates 1:9. All dilutions are normalized in the results. Absorbances were read at 450 nm and 570 nm. The absorbances read at 570 nm were subtracted from the absorbances read at 450 nm to remove background noise. Prism was used to generate the standard curve and calculate ferritin values for each condition. XLMiner Analysis ToolPak was used to conduct single-way ANOVA, which determined the p-values discussed in the results.

Ferritin Immunofluorescence and Confocal Imaging

After culturing on the scaffolds for 2 weeks, the cells were subjected to 150 μM of ferrous ascorbate, as described above. The cells were then incubated for 3 hours when the media was refreshed as described above. The cells incubated

further for a total of 24 hours. Then the cells were fixed, penetrated, and blocked as described above in the previous immunofluorescent staining section. After blocking, the ferritin monoclonal antibody (mouse, Thermofisher) was added to the cells at a 1:100 ratio. The cells then incubated at room temperature for 3 hours. Next, the secondary antibody, Alexa Fluor 488 goat-anti-mouse (Invitrogen), was added after washing the primary from the scaffolds with DPBS 3x. The cells were counterstained with DAPI. The cells were then incubated for 45 minutes at room temperature in the dark, and then washed with DPBS 3x and kept at 4°C until imaged.

Before confocal imaging, the scaffolds were trimmed to better expose the luminal surfaces. The luminal surfaces were observed and imaged using a Leica SP confocal microscope. The filters used were for DAPI (Ex/Em: 350/470 nm), and GFP/FITC (Ex/Em: 488/514 nm). To create the 3D rendered images, Leica confocal software (application X, 3.3.0.16799 and ImageJ) was used.

PicoGreen dsDNA Quantification

To normalize ferritin results, the number of cells/DNA on each scaffold needed to be determined. The kit used was the Quant-iT™ PicoGreen™ dsDNA Assay Kits and dsDNA Reagents (Invitrogen). Samples without exposure to iron but were cultured on scaffolds in parallel to the other scaffolds that were exposed to iron were used for this experiment. They were extracted at the same time and in the same manner as previously described. A standard curve was prepared as the kit specified and used to calculate all results. After preparing the samples as the

kit indicated, the fluorescence of the samples was read with excitation set to 480 nm and emission set to 520 nm. dsDNA was quantified as the kit described. After normalizing results with ferritin data, XLMiner Analysis ToolPak was used to conduct single-way ANOVA, which determined the p-values discussed in the results.

Results

Consistency Between Scaffolds

We ensured that each scaffold produced a well-defined 3D villi structure with uniform spacing and dimensions, while also preventing any damage to the delicate structure. To ensure quality, we conducted SEM imaging to capture high-resolution images of the luminal surface and identify any defects or irregularities in the 3D villi structure. The preparation of scaffolds for SEM was optimized as seen by the results in Figure 4.

Figure 4A shows one scaffold from the first batch of scaffolds (prepared by air-drying overnight after removing them from the molds) that was able to be coated with 10 nm of Pt/Pd. The others in this batch were unable to be coated with Pt/Pd because the sputter sensed liquid was still on the surface of the scaffolds and would not coat the samples. The scaffold in Figure 4A shows that the scaffold silk film is still primarily intact, and the villi are all accounted for. However, the SEM clarity and focus could be improved by better drying the scaffolds.

Figure 4B shows a flat scaffold with multiple rows of villi from the second batch of scaffolds that dried at -20°C and was submerged in 70% ethanol for an hour, 90% ethanol for an hour, 100% ethanol for two hours (changing the ethanol every hour), and finally reached the critical drying point at room temperature using HMDS. Both Figure 4Bi and 4Bii show how the villi became shriveled and misshapen, especially in comparison to Figure 4A.

Figure 4C shows a curved scaffold with multiple rows of villi from the final batch of scaffolds that dried by submerging them in 30% ethanol for an hour at 4°C, 50% ethanol for an hour at 4°C, 70% ethanol for an hour at -20°C, 90% ethanol for an hour at -20°C, 100% ethanol for two hours (changing the ethanol every hour) at -20°C, and finally reached the critical drying point at room temperature using HMDS. The villi seem to be less shriveled and mishappen, however, some villi were ripped out during the removal from the PDMS molds. The silk film seems to be mostly maintained, with cracks/holes in some places.

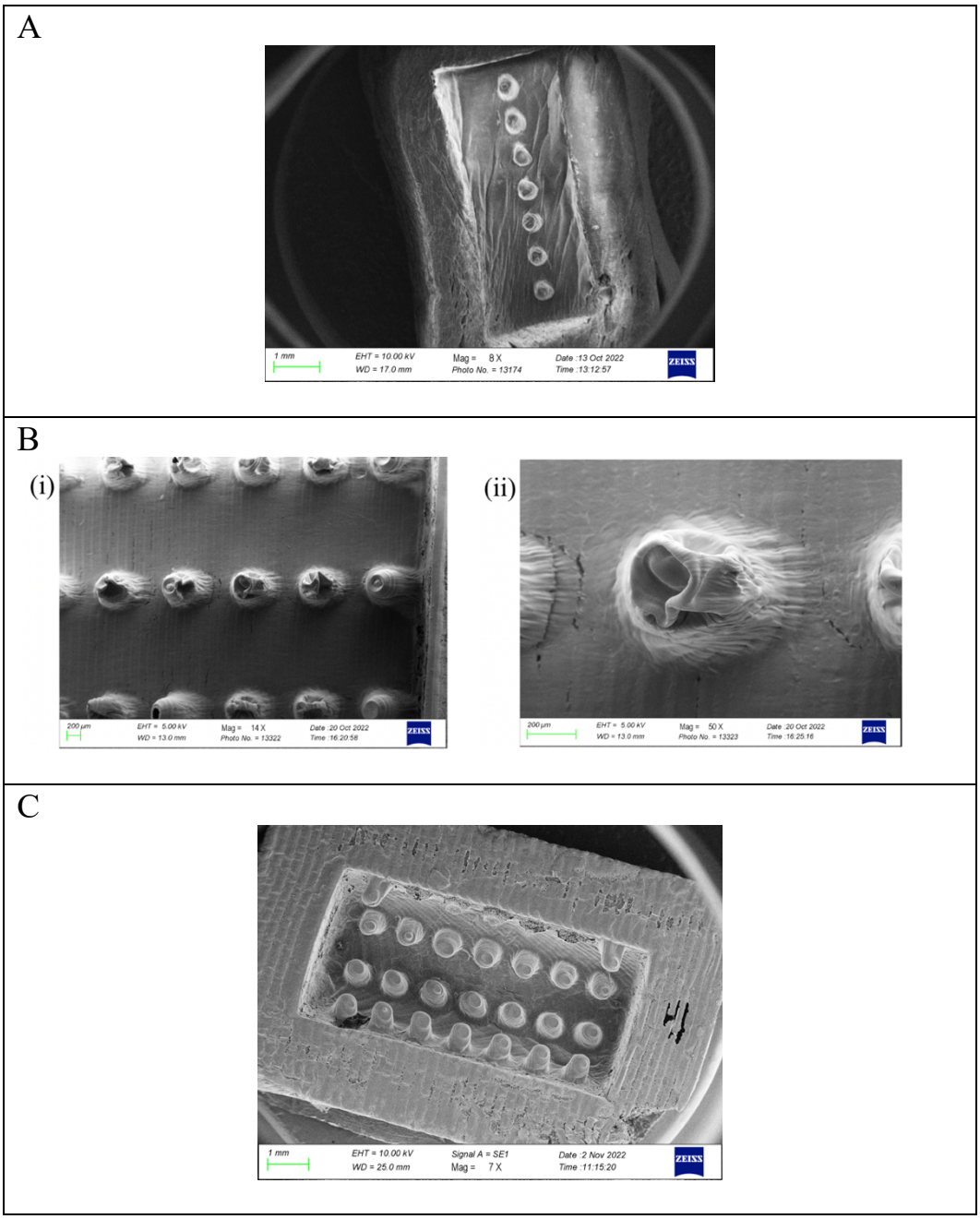

Figure 4. Scaffold SEM Pre-Preparation Trial Examples. (A) SEM images of a curved scaffold with one row of villi. This scaffold was air-dried overnight prior to SEM (Scale bar: 1 mm). (B) (i) SEM images of a flat scaffold with multiple rows of villi. This scaffold was dried with increasingly high concentrations of ethanol starting with 70% ethanol and ending with 100% ethanol and finally dried at room temperature overnight with HMDS to achieve critical point drying (Scale bar: 200 µm). (B) (ii) 50x magnification of one of the villi on the flat scaffold (Scale bar: 200 µm). (C) SEM of a curved scaffold with multiple rows of villi. This scaffold was dried with increasingly high concentrations of ethanol starting with 30% and ending with 100% ethanol and finally dried overnight with HMDS to achieve critical point drying (Scale bar: 1 mm).

Despite optimizing the drying process, we observed variations in the villi formation of the scaffolds, which could impact their performance. As a result, we need to quantify the inconsistencies to ensure that the scaffolds meet our quality standards. The following scaffolds were prepared using the final method of drying described above. Figure 5A depicts a row of villi on a flat scaffold with villi that are all intact and consistent. These villi, once coated with collagen, were suitable for cells to attach to and grow on. The silk film surrounding the villi is also smooth and without holes, which would prevent cells from falling through the surface and into the sponge. Figure 5B shows villi that are shriveled (as seen by the orange arrow), however, there are no holes in the villi. The red arrows here point to cracks and holes in the silk film. Figure 5C shows holes in the tops of the villi (as seen by the yellow arrows) while there are also more cracks in the silk film (as seen by the red arrows).

A

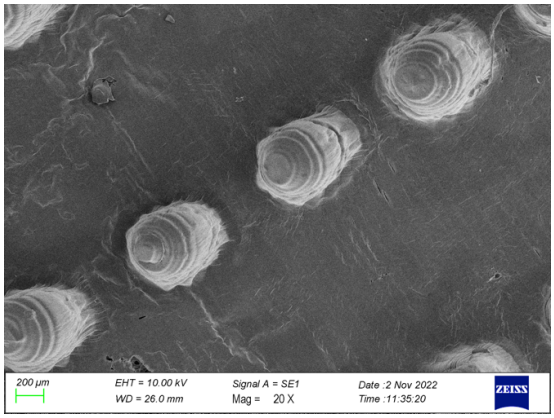

B

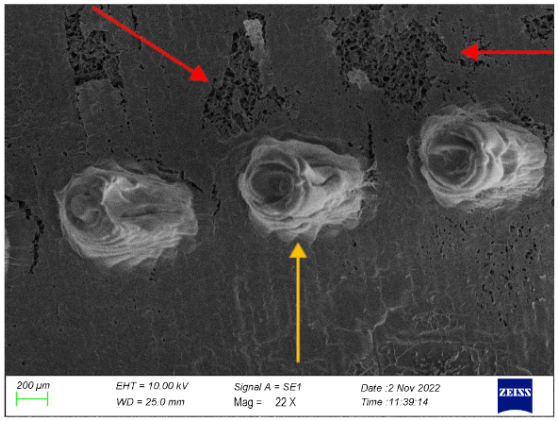

C

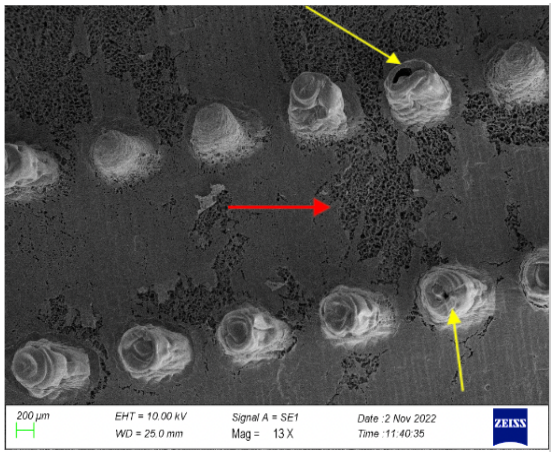

Figure 5. Inconsistencies between scaffolds shown on flat scaffolds with multiple rows of villi. (A) An example of good villi and silk film consistency. (B) An example of shriveling of villi (orange arrow) and cracks in the silk film (red arrows). (C) An example of holes in the villi (yellow arrows) and cracks in the silk film (red arrows).

To quantify the villi inconsistencies, 10 flat scaffolds with multiple rows of villi were created and prepared using the final method of drying described above and imaged using SEM. Figures 6A and 6B show one of the scaffolds in that batch at 5x magnification and 19x magnification, respectively. If there were holes in the villi that were significantly large, misshapenness of villi that was too severe, or the villus was missing altogether (as seen in the middle of the scaffold in Figure 6A), the villus was considered unusable. The holes and misshapenness were considered too severe if collagen would not cover efficiently their imperfections, likely affecting cell coverage and growth. The leftmost villus in Figure 6B, for example, was considered unusable due to its misshapenness.

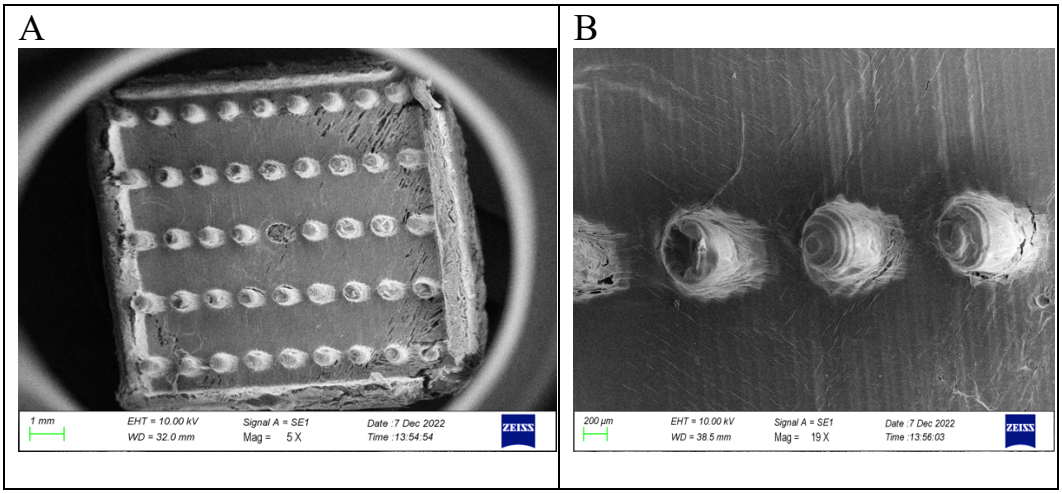

Figure 6. Example of scaffold created for inconsistency quantification. (A) Flat scaffold with multiple rows of villi whose unusable villi were counted to determine how many villi on average survive on a given scaffold. This scaffold had 3 villi considered unusable. (B) A closer look at three villi on the same scaffold. The leftmost villus was considered unusable due to drying having such a strong effect on the shape.

After counting all the unusable villi on the 10 scaffolds, the average was determined and subtracted from the total number of villi on each flat scaffold with multiple rows of villi. On average, 5 villi were unusable on a flat scaffold with

multiple rows of villi. The total number of villi on a flat scaffold with villi is 45 as seen in Figure 7. After subtracting 5 unusable villi, the total number becomes 40 villi. The surface area calculation was adjusted based on the new number of villi assumed to be usable on any given scaffold of this type. The survival rate of villi usability was determined to be 88.9% (40 was divided by 45). This value was multiplied by the total number of villi on each type of scaffold and the number of usable villi was adjusted as well as the surface areas as seen in Figure 7. There was no significant change in surface areas due to the adjusted villi values. There were still significant differences in total villi between flat with villi (40), curved with one row of villi (6), and curved with multiple rows of villi (25). Therefore, the consistency of these scaffolds was sufficient to enable the evaluation of the impact of villi on nutritional absorption, despite some variability in their quality.

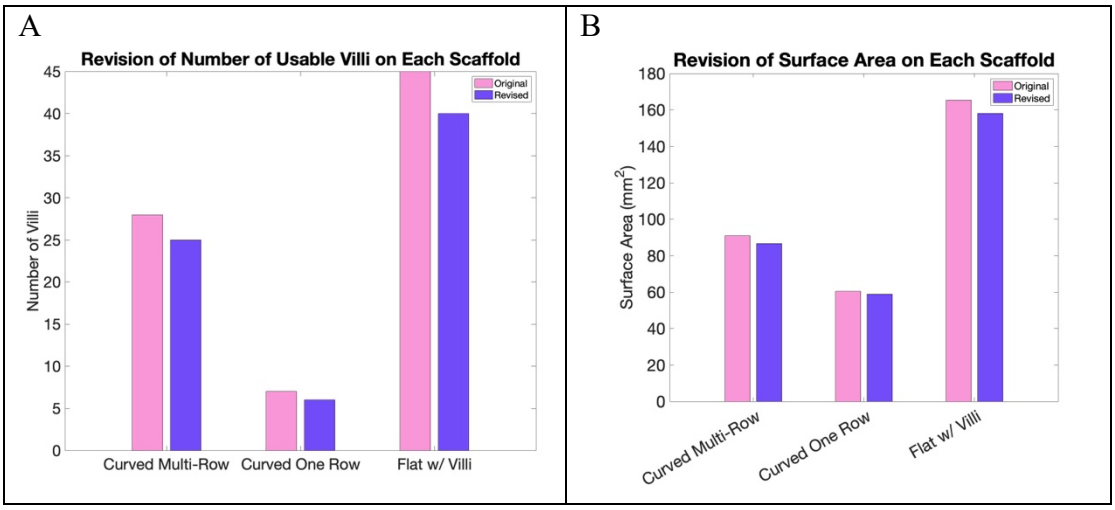

Figure 7. Adjusted scaffold surface areas based on villi usability survival rate. The usability survival rate of villi was 88.9%. (A) This value was used to determine the number of usable villi seen above. (B) The surface areas were recalculated with these news villi values.

3D Silk Scaffold Support of Cell Differentiation and Tissue Function

After 2 weeks of cell culturing, immunofluorescence showed that the epithelial tissue function of the cells on the scaffolds differentiated into heterogeneous populations of cells that expressed differentiation markers typical of the human intestinal epithelium. The differentiation markers typical of human intestinal epithelium include Zonula occludens (ZO)-1, mucin 2 (Muc-2), and sucrase isomaltase (SI). [29] The scaffolds were also imaged to illustrate total coverage and cell representation.

Figure 8A shows cell development and coverage on the villi. The cell polarization and tight junctions can be clearly seen on the villi in Figure 8Ai, due to the ZO-1 staining. The DAPI stain also shows complete cell coverage of the villi in both Figure 8Ai and 8Aii. Figure 8Bi and 8Bii show the cell differentiation and coverage in the lumen of the scaffolds. Figure 8Bi illustrates how there is far less tight junction development in the lumen of the curved scaffold, but equal cell coverage. Similarly, Figure 8Bii shows how even on the flat, smooth scaffold, not much tight junction or cell polarization could occur.

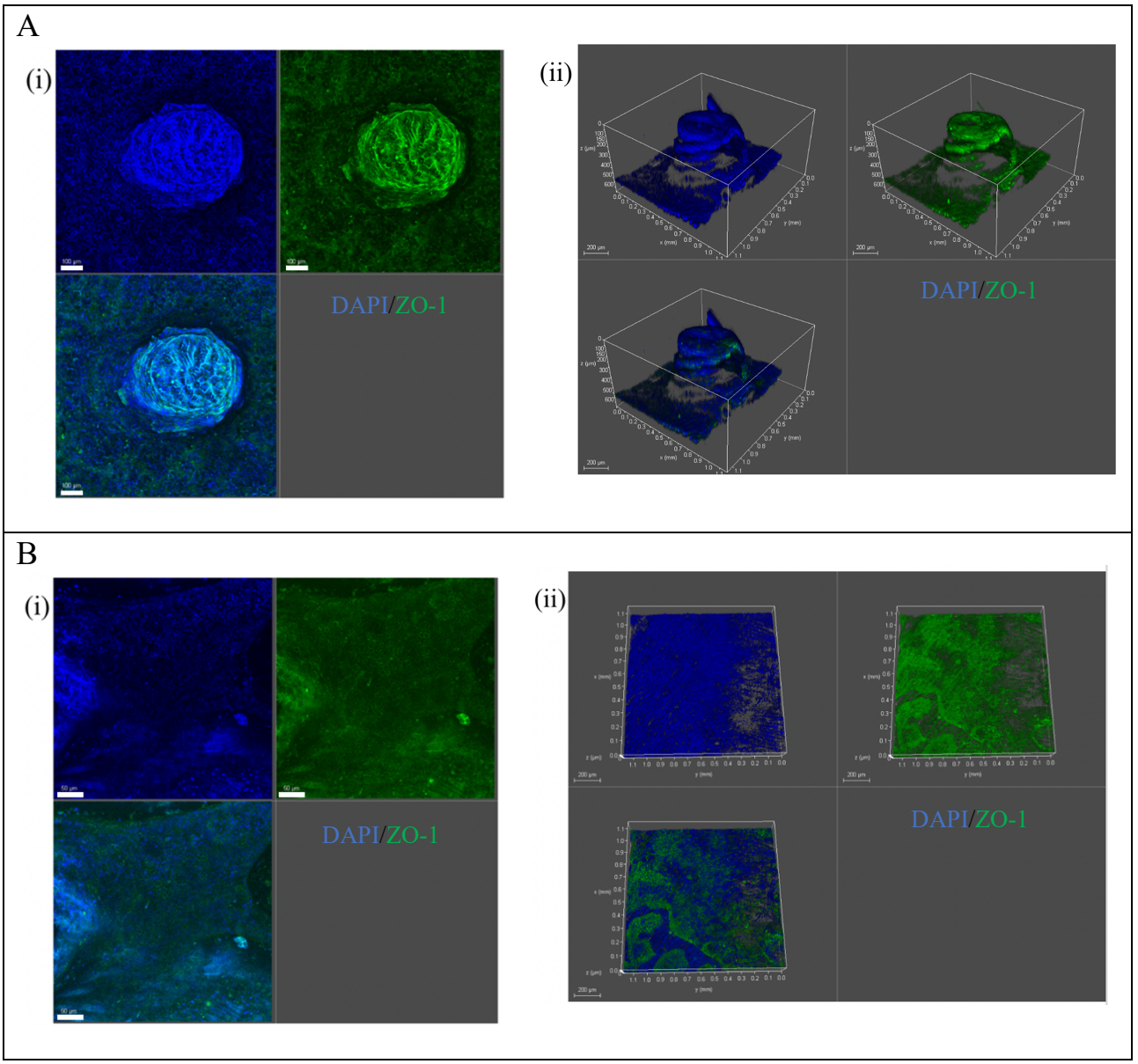

Figure 8. Confocal microscope images of scaffolds after two weeks of cell culturing stained with ZO-1 (green) and DAPI (blue). (A) (i) Confocal maximum projection fluorescence microscope images of villus on a flat scaffold with villi (Scale bar: 100 μm). (A) (ii) 3D reconstruction of z-stack of fluorescence microscope images of villus on a curved scaffold with multiple rows of villi (Scale bar: 200 μm). (B) (i) Confocal maximum projection fluorescence microscope images of lumen on a curved scaffold with one row of villi (Scale bar: 50 μm). (B) (ii) 3D reconstruction of z-stack of fluorescence microscope images of lumen on a flat, smooth scaffold (Scale bar: 200 μm).

Figure 9 shows the cell type representation and further differentiation after 2 weeks of cell culture on the 3D scaffolds. Figure 9Ai demonstrates how the

cells seemed to maintain their 4:1 initial seeding ratio as there are much more Caco-2 cells (enterocytes, SI) than the HT29-MTX cells (goblet cells, Muc-2). Further, Figure 9Aii illustrates how this representation is similar when looking at the same villus in a 3D reconstruction of z-stack fluorescence microscope images. In comparison, the lumen of flat, smooth scaffolds and curved, smooth scaffolds, as seen in Figure 9Bi and 9Bii respectively, also approximately reflect the 4:1 cell ratio of Caco-2 cells to HT29-MTX cells. Additionally, these images demonstrate full coverage on the scaffold, both on the villi and in the lumen.

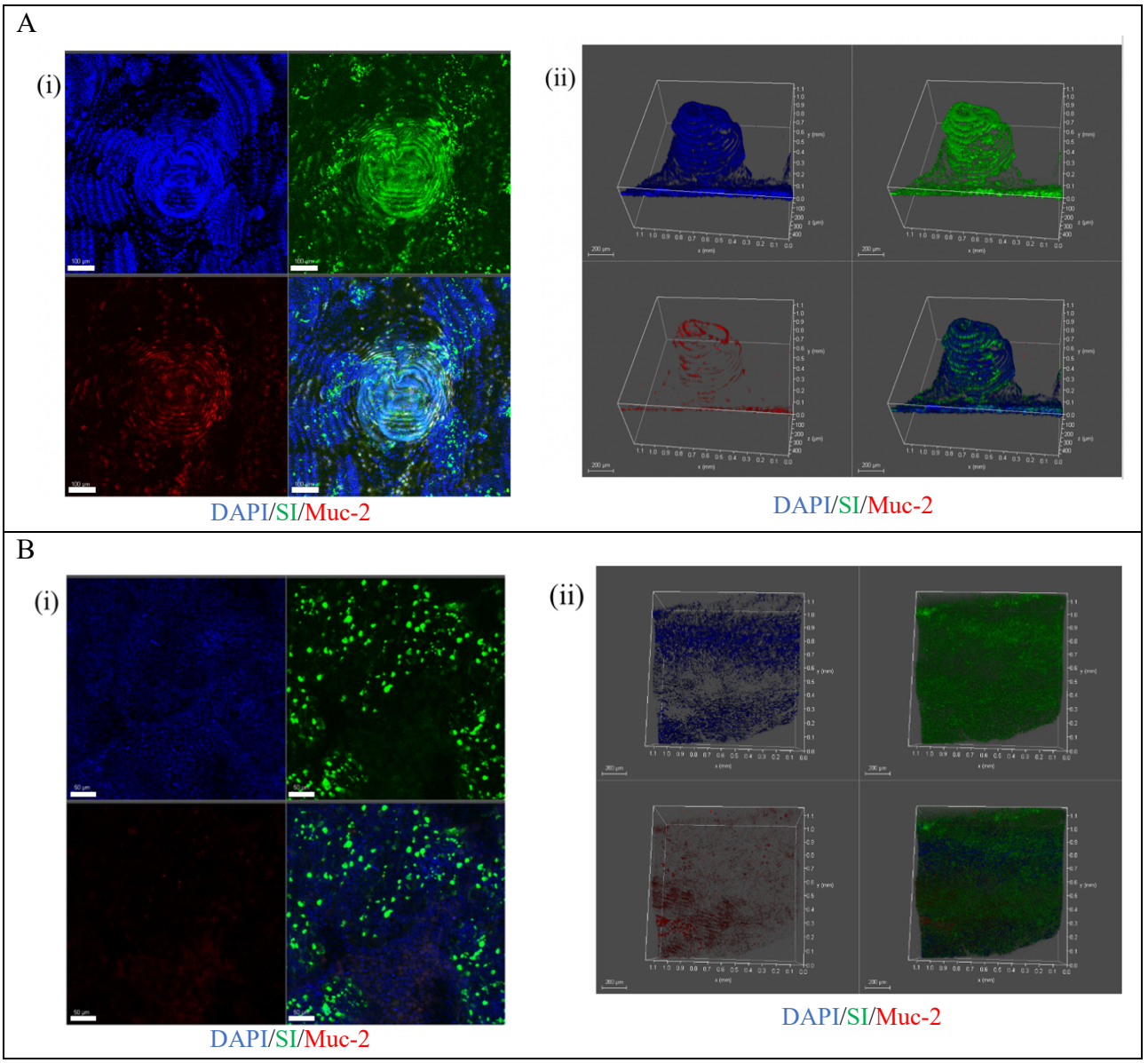

Figure 9. Confocal microscope images of scaffolds after two weeks of cell culturing stained with SI (green), Muc-2 (red), and DAPI (blue). DAPI is in blue to illustrate cell coverage, SI is in green to represent Caco-2 cells, and Muc-2 is in red to represent HT29-MTX cells. (A) (i) Confocal maximum projection fluorescence microscope images of villus on a flat scaffold with villi (Scale bar: 100 µm). (A) (ii) 3D reconstruction of z-stack of fluorescence microscope images of villus on a curved scaffold with multiple rows of villi (Scale bar: 200 µm). (B) (i) Confocal maximum projection fluorescence microscope images of lumen on a flat, smooth scaffold (Scale bar: 50 µm). (B) (ii) 3D reconstruction of z-stack of fluorescence microscope images of lumen on a curved, smooth scaffold (Scale bar: 200 µm).

Human Ferritin ELISA Optimization

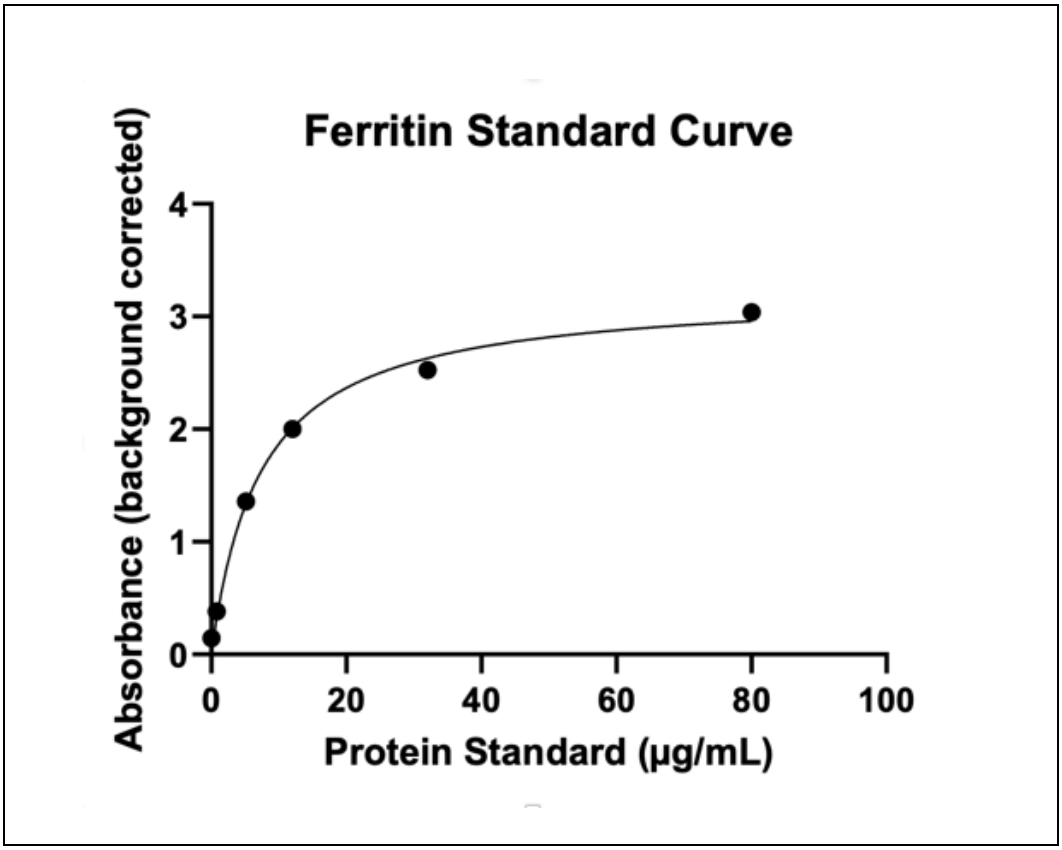

Figure 10. Standard curve of human ferritin ELISA. The standard curve was used in all ferritin calculations. The absorbance was corrected by subtracting the absorbance values read at wavelength 570 nm from the values read at 450 nm. All ferritin values recorded were corrected as well. The curve was fit to a sinusoidal shape as indicated by the kit. The R^2 value is .9921.

To ensure the ferritin values would be within the readable range of the standard curve, the optimal amount of iron needed to be added to the co-culture. Since only the Caco-2 cells are responsible for iron absorption, the optimization only used Caco-2 cells and they were cultured for a week on a 2D 48-well plate. The amount of iron analyzed was 0, 120, and 150 µM of ferrous iron. The ferrous iron was prepared as described above. A standard curve was prepared as indicated in ELISA kit instructions. Figure 10 shows the standard curve used to interpolate all ferritin values.

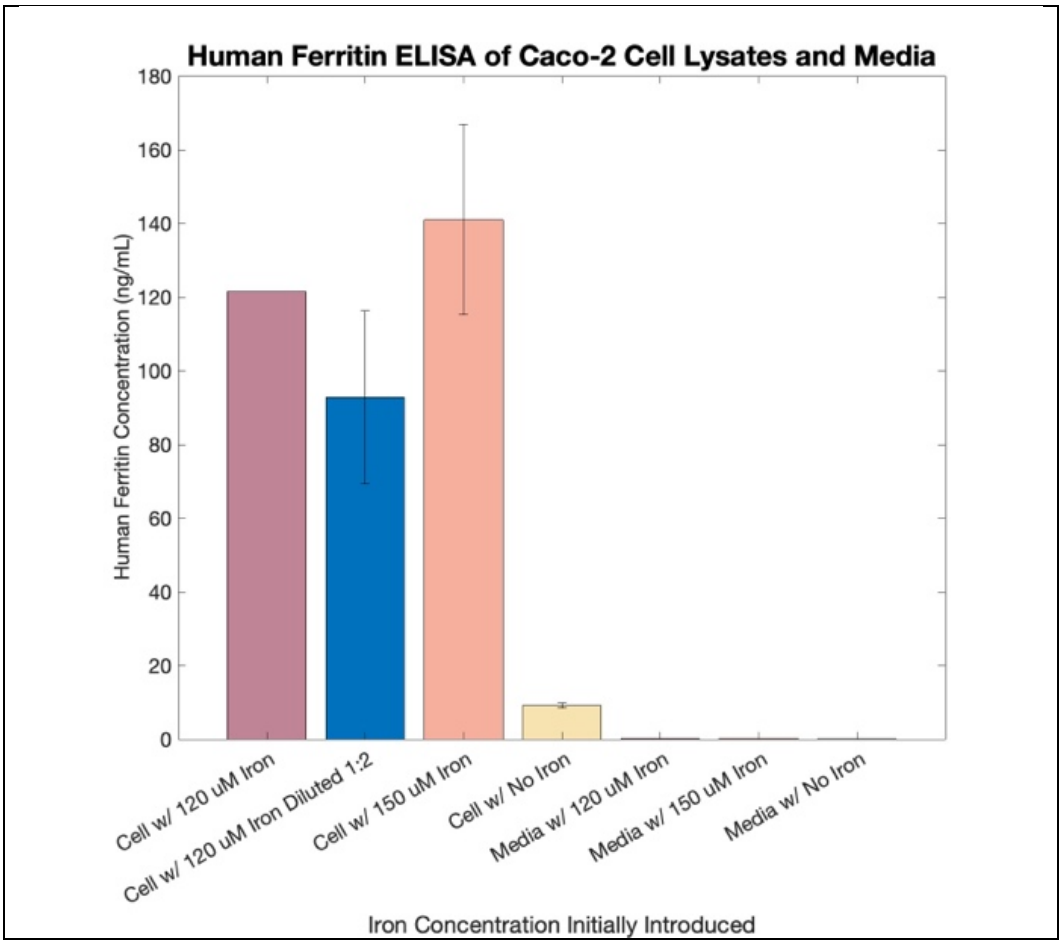

Figure 11. Cell lysate and media ferritin production. The first four bars in the bar graph show the amount of ferritin that was found in Caco-2 lysates after being subjected to 0, 120, and 150 μM of ferrous iron. The samples were diluted 1:1 prior to using the ELISA, except for the samples in blue that were introduced to 120 μM of ferrous iron which were diluted 1:2. The values presented are adjusted based on the given dilution. The "Cell w/ 120 μM Iron" bar does not have an error bar because only one value was obtained by the ELISA. This was because the other two values were out of the standard curve's range and could not be interpolated. There is no significant difference between the 120 μM ferrous iron sample that was diluted 1:2 and the 150 μM ferrous iron sample ($p > 0.05$). But there is a significant difference between the samples subjected to 150 μM ferrous iron and the samples subjected to no additional iron ($p < 0.05$). The next three bars represent the ferritin found in the media after the cells incubated 24 hours after their initial addition of iron. The media samples were not diluted. There is no significant difference between media sample ferritin readings ($p > 0.05$).

To determine whether to use the cell lysate and the media when calculating the total ferritin produced, Figure 11 shows the amount of ferritin found in the cell lysate and the media. Initially, the cell lysate values were diluted

1:1 while the media was not diluted prior to running the ELISA. Since the cells subjected to 120 μM ferrous iron produced absorbance values that were not within the standard curve, only one value was read as seen by the rose-colored, leftmost bar in Figure 11. In response to this, new cell lysate samples that were subjected to 120 μM ferrous iron were diluted 1:2 prior to conducting the ELISA. These values are shown by the blue bar in Figure 11. There was also much less ferritin found by the Caco-2 cells without any additional iron added in comparison to the samples subjected to 150 μM ferrous iron, as seen by the yellow bar and peach bar in Figure 11. Alternatively, when looking at the ferritin found in the media (the last three bars on the right) hardly any ferritin was found.

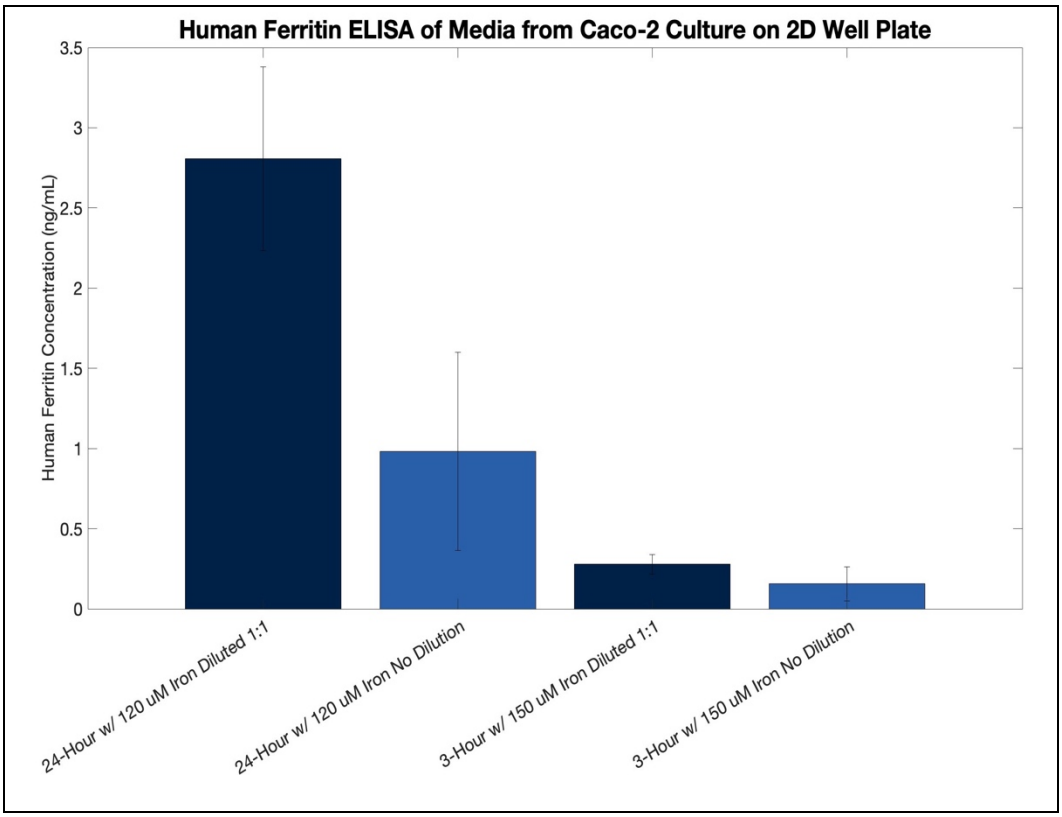

Figure 12. Media ferritin production. The amount of ferritin in the media used in Caco-2 cell culture on the 2D-well plate is recorded here. The left two bars show the media in culture 24 hours after the initial addition of 120 μM ferrous iron. The right two bars show the media in culture 3 hours after the initial addition

of 150 μM ferrous iron. The navy blue indicates a dilution of 1:1, while the lighter blue indicates no dilution. The values presented are adjusted based on the given dilution.

To see if diluting the media would affect the ELISA readings, some samples were diluted 1:1, as seen in Figure 12. The ferritin values were still all less than 4 ng/mL. However, diluting the media samples did produce higher ferritin values in comparison to the samples that were not diluted. In any case, the levels of ferritin in all media samples were found to be negligible compared to the cell lysate samples. As a result, moving forward, ferritin testing will be performed using cell lysate instead of media samples.

Human Ferritin Produced by Co-Cultures on 3D Silk Scaffolds: ELISA

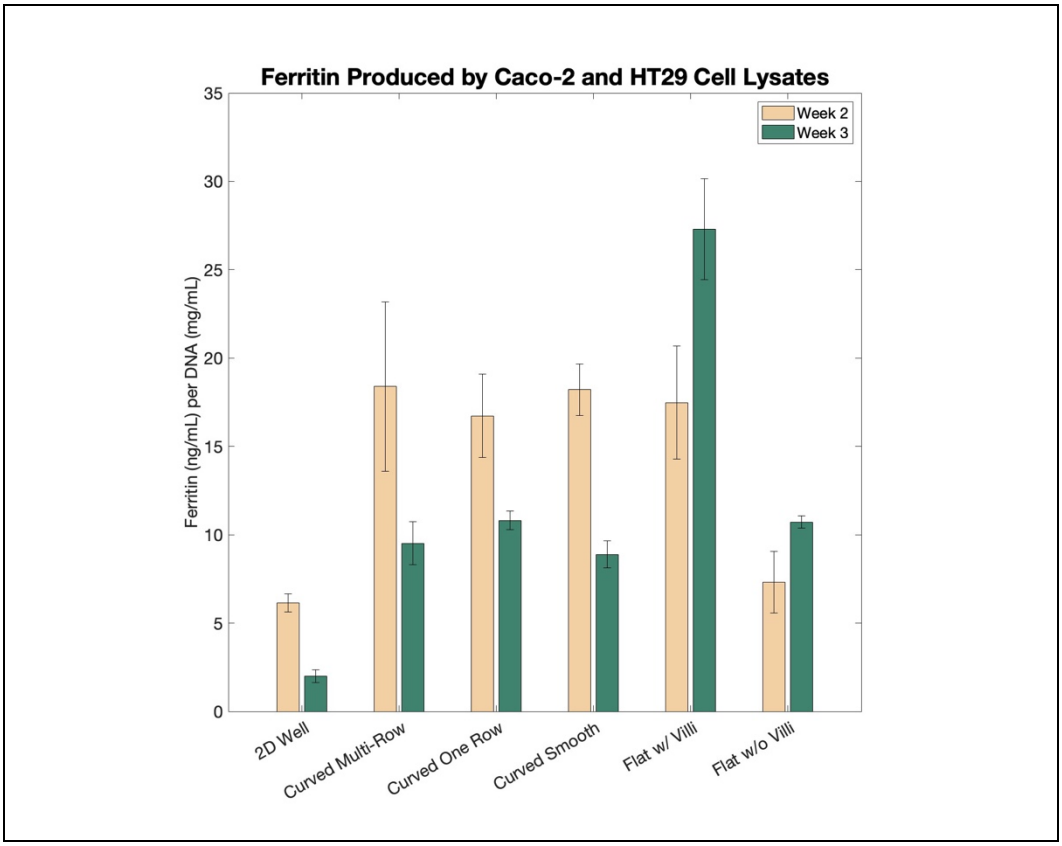

Figure 13. Human ferritin production from Caco-2 and HT29-MTX on silk scaffolds at weeks 2 and 3. The figure above illustrates the amount of ferritin

produced from each scaffold and 2D-well plate after 2 and 3 weeks of culturing. These values were determined by using a ferritin ELISA kit. The values were normalized by using a PicoGreen dsDNA quantification. Ferritin levels for the two types of flat scaffolds differ significantly from each other at weeks 2 and week 3 ($p < 0.05$). No significant difference in ferritin levels between curved scaffolds at weeks 2 and 3 ($p > 0.05$). Significantly different ferritin values for flat without villi and curved, smooth scaffolds in week 2 ($p < 0.05$), but not in week 3 ($p > 0.05$).

Figure 13 provided quantitative ferritin values to illustrate how the architecture of the small intestine affects iron absorption. Human ferritin ELISA was conducted on each of the cell lysates extracted from the scaffolds as described above. The sample lysates were diluted 1:2 prior to conducting the ELISAs. The values in Figure 13 are corrected based on this dilution. To show approximately show how much ferritin was produced per cell, the ferritin values were normalized by conducting a PicoGreen dsDNA quantification. After quantifying the DNA in each sample, to normalize the data, the ferritin values were divided by the total amount of dsDNA to show the ferritin produced per DNA (approximating ferritin produced per cell).

When looking at the week 2 ferritin values in comparison to the week 3 ferritin values, there was a more distinct trend in week 3. For example, in week 2, the flat scaffold with villi and the curved scaffolds all seem to show that the cells were producing similar amounts of ferritin. However, in week 3, the flat scaffold with villi produced much more ferritin than the other samples and much more than the previous week. Additionally, in both weeks 2 and 3 the flat scaffold with villi produced ferritin more efficiently than the smooth, flat scaffold. This fact indicates that the villus structures play a vital role in iron absorption. Conversely, there were significantly different ferritin values for the flat without villi and

curved, smooth scaffolds in week 2, but not in week 3. More specifically, in week 2 the curved scaffolds produced much more ferritin than the flat, smooth scaffolds. The curved scaffolds also all produced about the same amount of ferritin as each other in weeks 2 and 3.

Human Ferritin Produced by Co-Cultures on 3D Silk Scaffolds:

Immunofluorescent Stains

A. Flat w/ Villi Scaffold

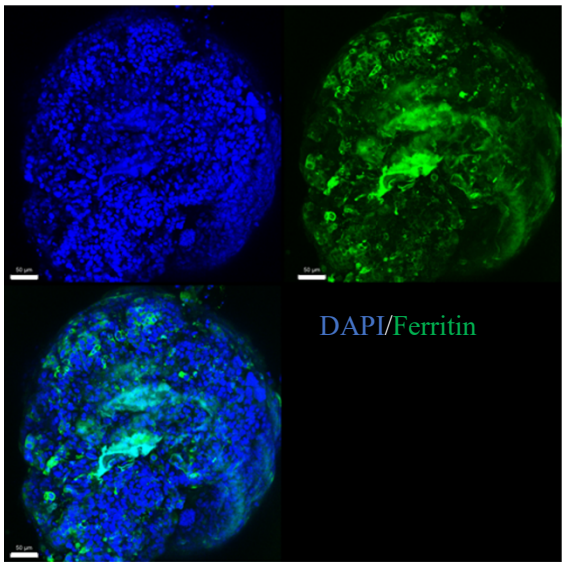

B. Flat and Smooth Scaffold

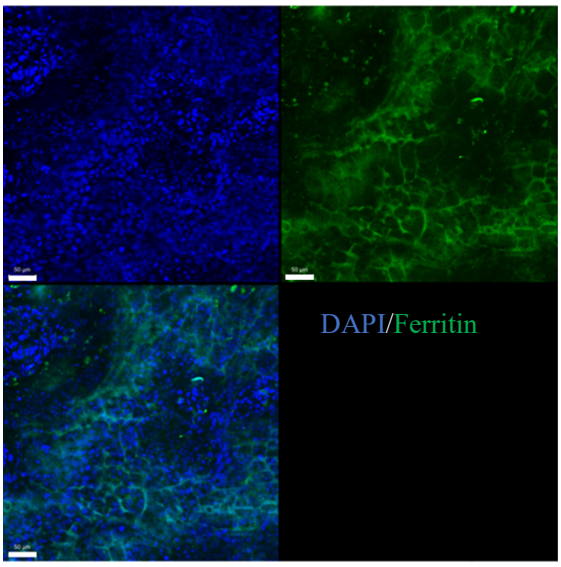

C. Curved with Multiple Rows of Villi Scaffold

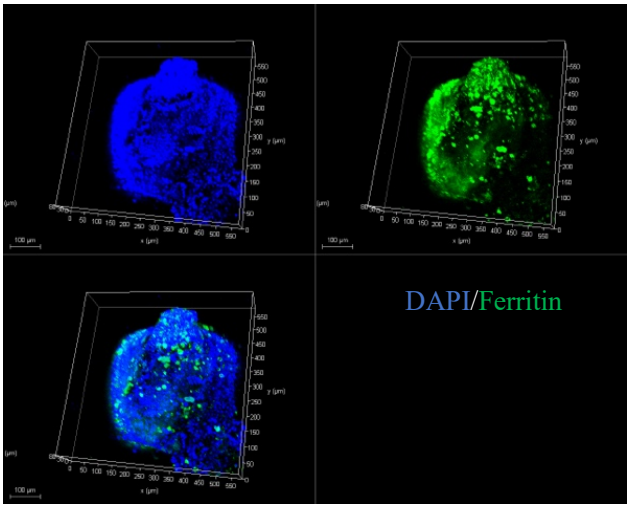

D. Curved with 1-Row of Villi Scaffold

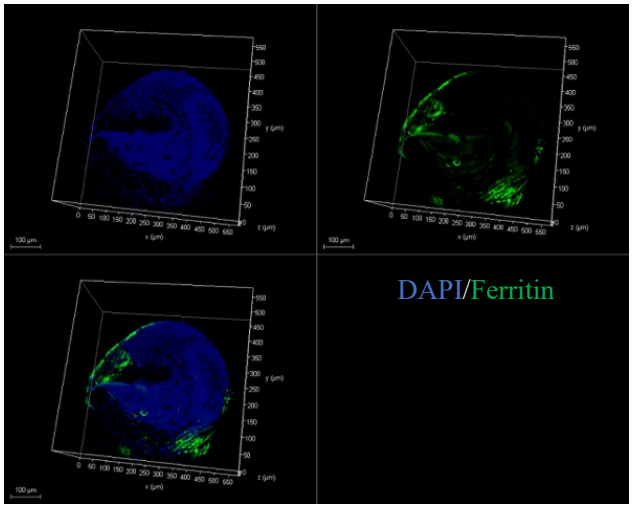

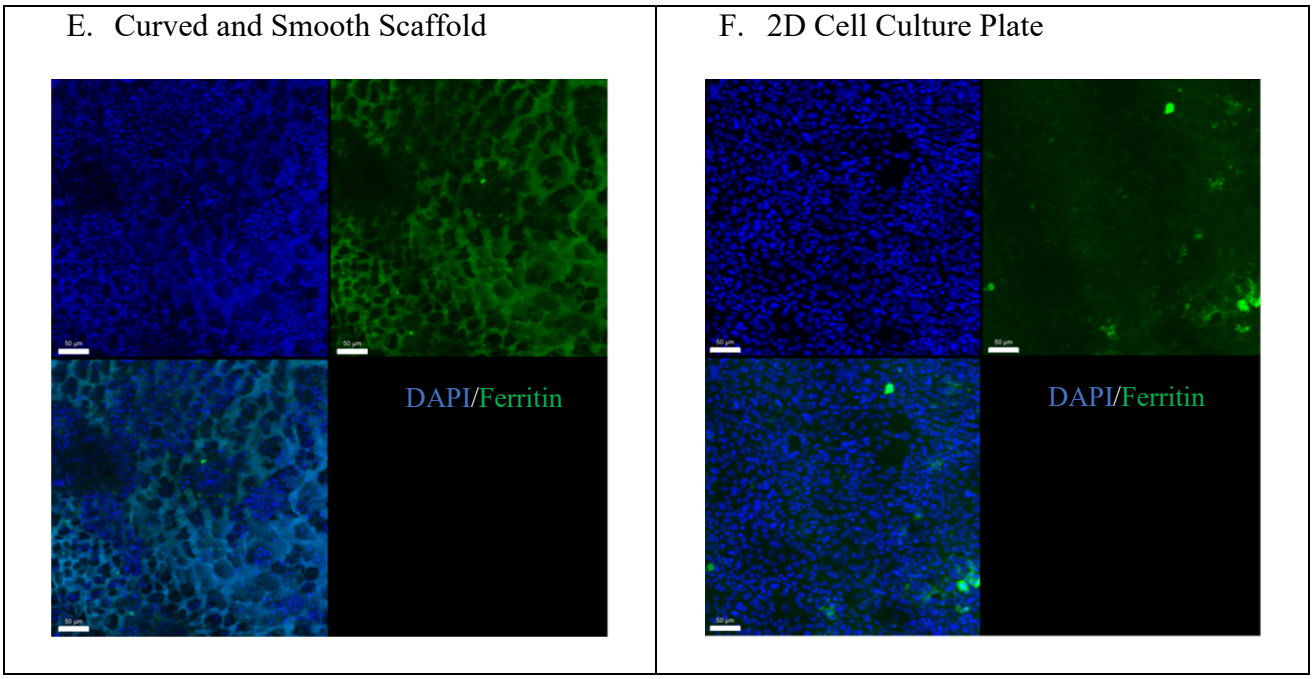

Figure 14. Immunofluorescent images showing ferritin production by co-culture on silk scaffolds after 2 weeks of culturing. All scaffolds and 2D well plates were stained with DAPI in blue and ferritin monoclonal antibody in green. All scaffolds and 2D well plates were seeded initially with Caco-2 and HT29-MTX cells at a 4:1 ratio. (A, C, D) Villus on the specified silk scaffold. (B, E) Lumen on the specified silk scaffold. (F) Cells on a 96-well plate. (A, B, E, F) Confocal maximum projection fluorescence microscope images (Scale bar: 50 μm). (C, D) 3D reconstruction of z-stack of fluorescence microscope images of specified scaffold (Scale bar: 100 μm).

To visualize ferritin production in the silk scaffolds, a ferritin monoclonal antibody was used. Figure 14 shows the confocal microscope immunofluorescent images that were obtained. Complete cell coverage was shown by the DAPI stain, while specific, defined green indicates ferritin production in those areas. Elevated levels of ferritin were observed in villi, while low levels were observed in the lumen/smooth surfaces (Figure 14). The specific ferritin binding could be more clearly seen in villi by the bright, green dots that formed (Figures 14A and 14C). The 1-row of villi scaffold showed streaks of green that were equally as bright, which could indicate ferritin production as well. This fact supports the data

illustrated in Figure 13 which indicates that the villus structures play a vital role in iron absorption. The lumen of the flat, smooth scaffold and the curved, smooth scaffold did not have much specific ferritin production and showed much dimmer signals (Figures 14B and 14E). The 2D-well plate showed some specific ferritin binding, but not nearly as much as the scaffolds with villi (Figure 14F).

Discussion

Scaffold Consistency

After optimizing the drying procedure of the scaffolds, it was determined that some mishappening of the villi may have been impacted by the drying method. The third drying method seemed to work the best, as it produced less aggressive shriveling overall and all the scaffolds could be coated with gold.

Studies have established criteria for "good" villus tips. A few studies found that in addition to taking trans-epithelial electrical resistance (TEER) readings, ZO-1 staining is a well-practiced way of establishing tight junction formation around the villi. [30,31] This would indicate that the formed barrier tissue started to mature in terms of cellular differentiation and polarization, which can only occur when cells grow up villus structures. [30] Similarly, other studies have tested both villi with curved tops and villi with flat tops. [12,32] Both studies have shown through TEER, ZO-1 stains, and metabolic activity assays that if the villi have a significant height difference from the lumen and an establish extra-cellular matrix, such as collagen, this will have a synergistic effect on intestinal cell differentiation and behavior. [12,31]

In this study, the villi height was designed to be 800 microns tall, and collagen was used as the ECM support. The heights of the villi in the studies previously mentioned were between 120 microns and 800 microns. [30,32,33] All studies were able to see a significant effect the villi had on cell development. [30,32,33] Physiologically, villi in vivo range from about 0.2 to 1 mm in length. [34] Therefore, extreme misshapenness that causes the villi to be less than 120 microns tall or the villus to be missing altogether affects cell differentiation. This created the need to quantify the number of unusable villi on each scaffold to ensure an accurate interpretation of results in later experimentation.

In this study, not all the scaffolds were produced perfectly. Figures 5 and 6 show that not all inconsistencies are equal. Occasional defects, such as cracks and holes, were observed in the silk film. However, this issue was addressed by applying a collagen coating before seeding cells onto the scaffold. The necessary support of the collagen layer was demonstrated by previous studies. [31] The findings were further supported by the observations made in Figure 8B, where complete cell coverage was observed within the lumen, indicating that the cracks were reinforced by the underlying collagen layer. Similarly, most holes and minor mishappening on the villi cannot be considered an issue after being coated with a collagen layer. The collagen prevents the cells from falling through or into the scaffolds, while also providing smoothness to the shape of the villi. This was shown in Figure 8A as seen by both the total cell coverage on the villus and the structural integrity of the villus. While it is true that the cells may occasionally form a flatter monolayer at the top of the villus, research has indicated that

differentiation occurs as the cells migrate up the villi. As a result, the tight junction formations are unlikely to be affected by the cell arrangement at the villus apex, as demonstrated by previous studies. The ZO-1 stains in this study also were able to show tight junction formation like what has been seen in previous studies (Figures 8A and 8B).

Cell Growth and Differentiation on 3D Silk Scaffolds

Intestinal cell (Caco-2, HT29-MTX) attachment, growth, and *in* vitro culture support were demonstrated with cell polarization and differentiation (Figures 8-9). Previous studies have used immunofluorescent images to demonstrate the 3D silk scaffold's ability to support cell differentiation and accurately represent an *in vivo* human intestinal epithelium. [5,30] Particularly, ZO-1, Muc-2, and SI have been used for this purpose. [5,30] In this study, regardless of the type of scaffold, the z-stack reconstructions showed confluent monolayers of differentiated intestinal epithelia (Figures 8-9). Specifically, the Caco-2 cells produced distinct tight junctions and cell polarization, especially seen on the villi (Figure 8A), which was expected as seen in previous studies. [12,30] This is important because as Caco-2 cells differentiate into a monolayer of cells, they display many properties typical of absorptive enterocytes with brush border layer as found in the human small intestine. [15] Additionally, Figure 8 showed the Muc-2 staining of HT29-MTX cells, which confirmed the presence of a mucous-secreting cell line in the co-culture. [16] Thus, the scaffolds supported the co-culture

of Caco-2 cells and HT29-MTX cells confirming that the architectures supported intestinal epithelial cell adhesion, proliferation, and differentiation.

Optimization of Human Ferritin ELISA

Previous studies have investigated different iron concentrations for their *in vitro* small intestine models. [20-23,25] It is worth noting that all the aforementioned nutritional studies were conducted using 2D cell-culture systems. While several previous studies have simulated food digestion and then introduced the digested contents to their in vitro models [20,25], our tissue model focused solely on iron absorption. When looking at studies that only added ferrous iron, typically for 2D co-cultures in 24-well transwell plates, once the cells were confluent, ferrous ascorbate was added in concentrations between 10 μM and 200 μM. [22,23] Since our 3D co-culture system comprised a larger number of cells, we chose to test on the higher concentrations of ferrous ascorbate. Consequently, we evaluated the effects of 0, 120, and 150 μM concentrations to determine the optimal concentration for our final ELISA.

Based on the results in Figure 11, there was no significant difference between the ferritin found in the cells that were subjected to 120 μM ferrous iron and the 150 μM ferrous iron, and therefore,150 μM ferrous iron was used in the following experiments. Because the difference between the ferritin values obtained from the samples with no additional iron added was much less than the ferritin values obtained from the samples with 150 μM ferrous iron added, this also confirms 150 μM ferrous iron would be a reasonable amount of iron to add to

the co-culture when testing this iron absorption model. Furthermore, the samples obtained in the following experiments were diluted 1:2, to ensure that the absorbance values would remain within the standard curve (Figure 11).

Additionally, no media was used to record ferritin values in the following experiments since the values were so low in comparison to the cell lysate ferritin values (Figure 12). Some other studies have included ferritin collected in the media as part of their overall ferritin evaluation, but most only include the cell lysate. [17,21,22] It is possible that the low readings obtained from the ELISA kit for ferritin were because the protein was already highly diluted by the media. Thus, 150 μM ferrous iron was added to the co-cultures in the following experiments, and the cell lysates were used to quantify ferritin production. The samples were also diluted 1:2 prior to conducting the ELISAs.

Human Ferritin Produced by Co-Cultures on 3D Silk Scaffolds

Based on the immunofluorescent images and the ferritin ELISA, it seems that ferritin was produced more efficiently in the villi, while the curvature of the scaffolds did not seem to assist in ferritin production efficiency. From a physiological standpoint, it makes sense that the cells in the villi would have higher nutrient absorption capabilities because they are closest in the small intestine to nutrients that flow through. [12] This idea is supported by previous literature which shows there is a significant difference in differentiation levels in the villi than in the lumen. [31] Additionally, as stated previously, Figure 8A also showed the development of a brush border layer (presence of defined tight

junctions) on the villi whereas it was not as present in the lumen. This means that the protrusion of the villi structures certainly encourages tight junction formations, the formation of a brush border layer, and the establishment of more efficient nutrient absorption by enterocytes and Caco-2 cells. [12]

Furthermore, Figures 13 and 14 show that villus structure integrity is the biggest determinant of iron absorption efficiency. This was shown by the specific ferritin binding of the ferritin monoclonal antibody in the villi in comparison to the dimmer signal in the lumen. Additionally, the ELISA data showed a significantly higher amount of ferritin production in the flat scaffold with villi than in the smooth, flat scaffold in weeks 2 and 3.

In comparison, the lumen curvature had far less evidence showing its effect on iron absorption. Not only did the immunofluorescent images show less specific ferritin binding and less tight junction development, but there was no conclusive evidence showing that the curvature had much of an effect on nutritional absorption, as seen by the difference in ferritin production between the smooth, curved scaffolds and the smooth, flat scaffolds in weeks 2 and 3. One could argue that curvature has a small effect on iron absorption because in week 2 the smooth, curved scaffold produced significantly more ferritin. Still, more evidence would need to be obtained because week 3 showed no difference between the groups. On the other hand, this could have been because the cell density at week 3 had become over-confluent and caused some of the cells to die off or reduce in metabolic efficiency, whereas the flat scaffold had more space for cells to develop. Or perhaps the curvature of the scaffold was not significant

enough to cause an impactful effect on nutritional absorption. These adjustments could be explored in future studies. Ultimately, this model can be used to model iron absorption and potentially other nutrient absorption as well.

Interestingly, there was also no significant difference in the ferritin levels between curved scaffolds at weeks 2 and 3. The combination of villi and curvature would suggest that this type of scaffold would produce ferritin most efficiently. However, a potential reason this occurred may be due to the cells not overproducing on the scaffolds, reducing their metabolic capabilities while there was much more surface area on the flat scaffolds. Lowering the initial cell density during seeding could potentially allow for total scaffold coverage at the end of the two-week period without compromising cell viability by limiting cell-to-cell contact. However, despite this approach, it was found that isolating the architectural features proved to be an effective means of determining the individual impact of each feature on nutritional absorption.

Conclusion

In this study, an *in vitro* model of the small intestine was analyzed to test whether it could be used as a method to model nutritional absorption and identify what architectural features of the small intestine most affect nutritional absorption. The features of the small intestine analyzed were the villus structures and curvature of the lumen. To test these features, 3D silk scaffolds were made both isolating and combining these features. This methodology of creating the scaffolds was then verified through SEM with the support of previous literature.

[12,12,31,32] This was also proven to be successful as seen by the immunofluorescent images that showed total cell coverage by a monolayer of co-cultured Caco-2 and HT29-MTX cells. The consistency between scaffolds villi was established to be 88.9%. This value was considered and the new average number of villi on a scaffold was established. The scaffolds were thus established to be a verified model to support intestinal cell differentiation, cell representation, and metabolic activity.

This study determined that the villus structures play an essential role to iron absorption. From a physiological standpoint, this seems logical since the villi are most in contact with the nutrients that flow through the small intestine. Additionally, the most differentiated cells are at the top of the villi. This study showed that Caco-2 cells would not differentiate and form tight junctions, without the presence of villi. The villi caused the Caco-2 cells to display properties typical of absorptive enterocytes with a brush border layer as found in the human small intestine. By then adding 150 μM ferrous iron to the co-cultures, the evidence of villi importance became clearer. The ELISA and ferritin monoclonal antibody stains showed higher levels of ferritin production and specific ferritin binding in scaffolds with villi, while the smooth scaffolds and luminal linings all showed little ferritin production rates and binding. In conclusion, a novel method for analyzing iron absorption was established. However, the impact of luminal lining curvature on nutritional absorption remains an area that requires further investigation. Future studies in this area could provide valuable insights into the

role of luminal lining curvature in nutrient absorption and the development of physiologically relevant models for studying intestinal function.

Future Directions

The next step would be to test whether this *in vitro* model can be used to study other types of nutritional absorption. For example, a potential nutrient to study could be histidine. Histidine would be a good nutrient to study using this model because it would show this model can be used to study amino acid uptake and potentially protein absorption. Peptide transporters are also predominately expressed in intestinal epithelial cells. [35] Thus, histidine would also be a strategic choice because Caco-2 cells are known to express specific peptide histidine transporters that mediate histidine uptake. [35] From a nutritional perspective, histidine is an essential amino acid, meaning we must obtain this nutrient from our diets since it is not synthesized by mammals. [36] Therefore, histidine would be a relevant nutrient to study using this model and one could do this by using the same types of cell lines.

If one could model protein absorption or other types of nutrients using this model, it would also have the potential ability to compare nutritional absorption from the consumption of real meat to artificially grown meat. Cellular agriculture is a growing field of interest, as the need for manufacturing food without plant or animal involvement becomes incessantly pressing. Traditional agriculture may be sufficient now, however, as the world population increases to as much as 11 billion by the year 2050, the ability to supply enough food while also under the

pressure of limited arable land and climate change becomes uncertain. [37] In addition to supporting food supply through cellular agriculture alternatives, one also must ensure that the artificially grown food has the same or better nutritional makeup as traditional food. With labs focused on cultivating meat, dairy, eggs, and many other sources of food through cellular agriculture techniques, this model could be used to assess and further verify and validate their sustainability as a food source alternative.

Another potential next step would be to test this 3D silk scaffold model using another type of intestinal cell line. Intestinal organoids can partially recapitulate the identity, cell heterogeneity, and cell behavior of the original tissue in *in vitro* models. [38] They are much more difficult to maintain and culture, however, which may prove to be a challenge with this model. [38] Still, organoids would be preferred over transformed cancer cell lines, such as Caco-2, because transformed cells fail to fully recapitulate the normal physiology and lineage development of the native intestinal epithelium. [38] Organoids can accomplish these requirements.

Finally, this *in vitro* tissue model has the potential capacity to model drug absorption. If one were to seed this 3D silk scaffold model with diseased cells such as celiac or inflammatory bowel disease (IBD) cells, one could analyze the efficacy of drug absorption and determine the most optimal medication before the patient is even prescribed. First, one would have to confirm the diseased cells were behaving as they would *in vivo*. Next, the drug could be tested on the diseased cells in the model and assist in providing pre-clinical evidence to support

the next step of clinical *in vivo* drug testing, if still required before the drug can be prescribed to the public. This would depend on the accuracy of the *in vitro* modeling. Regardless, this *in vitro* model has many applications in biomedical fields, ranging from cellular agriculture to drug delivery modeling, which may spur new possibilities in research and clinical applications.

References

1 Bodinier, M. *et al.* Intestinal Translocation Capabilities of Wheat Allergens Using the Caco-2 Cell Line. *Journal of Agricultural and Food Chemistry* **55**, 4576-4583 (2007). https://doi.org:10.1021/jf070187e

2 Wang, Y.-J. *et al.* Irradiation Induced Injury Reduces Energy Metabolism in Small Intestine of Tibet Minipigs. *PLOS* (2013). https://doi.org:https://doi.org/10.1371/journal.pone.0058970

3 Mullin, G. E. & Swift, K. M. *The Inside Tract: Your Good Gut Guide to Great Digestive Health*. (2011).

4 Kim, W. & Kim, G. H. An intestinal model with a finger-like villus structure fabricated using a bioprinting process and collagen/SIS-based cell-laden bioink. *Theranostics* **10**, 2495-2508 (2020). https://doi.org:10.7150/thno.41225

5 Rudolph, S. E. *et al.* Crypt-Villus Scaffold Architecture for Bioengineering Functional Human Intestinal Epithelium. *ACS Biomaterials Science & Engineering* **8**, 4942-4955 (2022). https://doi.org:10.1021/acsbiomaterials.2c00851

6 Wang, Y. *et al.* A microengineered collagen scaffold for generating a polarized crypt-villus architecture of human small intestinal epithelium. *Biomaterials* **128**, 44-55 (2017). https://doi.org:https://doi.org/10.1016/j.biomaterials.2017.03.005

7 Roostaee, A., Benoit, Y. D., Boudjadi, S. & Beaulieu, J. F. Epigenetics in Intestinal Epithelial Cell Renewal. *Journal of Cellular Physiology* **231**, 2361-2367 (2016). https://doi.org:10.1002/jcp.25401

8 Kisielinski, K., Willis, S., Prescher, A., Klosterhalfen, B. & Schumpelick, V. A simple new method to calculate small intestine absorptive surface in the rat. *Clinical and Experimental Medicine* **2**, 131-135 (2002). https://doi.org:10.1007/s102380200018

9 Kwon, O., Han, T.-S. & Son, M.-Y. Intestinal Morphogenesis in Development, Regeneration, and Disease: The Potential Utility of Intestinal Organoids for Studying Compartmentalization of the Crypt-Villus Structure. *Frontiers in Cellular and Developmental Biology* **8** (2020). https://doi.org:10.3389/fcell.2020.593969

10 De Angelis, I. & Turco, L. Caco-2 cells as a model for intestinal absorption. *Curr Protoc Toxicol* (2011). https://doi.org:10.1002/0471140856.tx2006s47
11 Kapałczyńska, M. *et al.* 2D and 3D cell cultures – a comparison of different
types of cancer cell cultures. *Arch Med Sci* **14**, 910-919 (2018). https://doi.org: https://doi.org/10.5114/aoms.2016.63743
12 Hewes, S. A. *et al.* In Vitro Models of the Small Intestine: Engineering Challenges and Engineering Solutions. *Tissue Engineering Part B: Reviews* **26**, 313-326 (2020). https://doi.org:10.1089/ten.teb.2019.0334
13 Costello, C. M. *et al.* Synthetic small intestinal scaffolds for improved studies of intestinal differentiation. *Biotechnol. Bioeng.* **111**, 1222-1232 (2014). https://doi.org:10.1002/bit.25180
14 Snoeck, V., Goddeeris, B. & Cox, E. The role of enterocytes in the intestinal barrier function and antigen uptake. *Microbes and Infection* **7**, 997-1004 (2005). https://doi.org:https://doi.org/10.1016/j.micinf.2005.04.003
15 Lea, T. Caco-2 Cell Line. *Springer, Cham* (2015). https://doi.org:https://doi.org/10.1007/978-3-319-16104-4_10
16 Qiu, J., Zhang, J. & Li, A. Cytotoxicity and intestinal permeability of phycotoxins assessed by the human Caco-2 cell model. *Ecotoxicology and Environmental Safety* **249** (2023). https://doi.org:https://doi.org/10.1016/j.ecoenv.2022.114447
17 Perfecto, A. *et al.* Mechanisms of Iron Uptake from Ferric Phosphate Nanoparticles in Human Intestinal Caco-2 Cells. *Nutrients* **9** (2017). https://doi.org:10.3390/nu9040359
18 Ross, A., Caballero, B., Cousins, R., Tucker, K. & Ziegler, R. *Modern Nutrition in Health and Disease*. 11 edn, 176-188 (Lippincott Williams & Wilkins, 2014).
19 Gianoukakis, A. G. *et al.* Characterization of the anemia associated with Graves' disease. *Clinical Endocrinology* **70**, 781-787 (2009). https://doi.org:10.1111/j.1365-2265.2008.03382.x
20 Christides, T., Ganis, J. C. & Sharp, P. A. In vitro assessment of iron availability from commercial Young Child Formulae supplemented with prebiotics. *European Journal of Nutrition* **57**, 669-678 (2016). https://doi.org:https://doi.org/10.1007/s00394-016-1353-3
21 Thompson, B., Sharp, P., Elliot, R., Al-Mutairi, S. & Fairweather-Tait, S. J. Development of a Modified Caco-2 Cell Model System for Studying Iron Availability in Eggs. *Journal of Agricultural and Food Chemistry* **58**, 3833–3839 (2010). https://doi.org:10.1021/jf904175d
22 Scheers, N. M., Almgren, A. B. & Sandberg, A.-S. Proposing a Caco-2/HepG2 cell model for in vitro iron absorption studies. *The Journal of Nutritional Biochemistry* **25**, 710-715 (2014). https://doi.org:https://doi.org/10.1016/j.jnutbio.2014.02.013
23 Glahn, R. P., Lee, O. A. & Miller, D. D. In Vitro Digestion/Caco-2 Cell Culture Model to Determine Optimal Ascorbic Acid to Fe Ratio in Rice

Cereal. *Journal of Food Science* **64**, 925-928 (1999). https://doi.org:10.1111/j.1365-2621.1999.tb15942.x

24 Timoshnikov, V., Kobzeva, T., Polyakov, N. & Kontoghiorghes, G. Redox Interactions of Vitamin C and Iron: Inhibition of the Pro-Oxidant Activity by Deferiprone. *International Journal of Molecular Sciences* **21** (2020). https://doi.org:10.3390/ijms21113967

25 Etcheverry, P., Wallingford, J. C., Miller, D. D. & Glahn, R. P. Calcium, Zinc, and Iron Bioavailabilities from a Commercial Human Milk Fortifier: A Comparison Study. *Journal of Dairy Science* **87**, 3629-3637 (2004).

26 Yun, S., Habicht, J.-P., Miller, D. D. & Glahn, R. P. An In Vitro Digestion/Caco-2 Cell Culture System Accurately Predicts the Effects of Ascorbic Acid and Polyphenolic Compounds on Iron Bioavailability in Humans *The Journal of Nutrition* **134**, 2717-2721 (2004). https://doi.org:https://doi.org/10.1093/jn/134.10.2717

27 Chen, Y. *et al.* Robust bioengineered 3D functional human intestinal epithelium. *Scientific Reports* **5**, 13708 (2015). https://doi.org:10.1038/srep13708

28 Chen, Y. *et al.* Bioengineered 3D Tissue Model of Intestine Epithelium with Oxygen Gradients to Sustain Human Gut Microbiome. *Advanced Healthcare Materials* **11**, 2200447 (2022). https://doi.org:https://doi.org/10.1002/adhm.202200447

29 Sinagoga, K. L. & Wells, J. M. Generating human intestinal tissues from pluripotent stem cells to study development and disease. *EMBO Journal* **34**, 1149-1163 (2015). https://doi.org:https://doi.org/10.15252/embj.201490686

30 Taebnia, N. *et al.* Dual-Material 3D-Printed Intestinal Model Devices with Integrated Villi-like Scaffolds. *ACS Applied Materials & Interfaces* **13**, 58434-58446 (2021). https://doi.org:10.1021/acsami.1c22185

31 Wang, L., Murthy, S. K., Barabino, G. A. & Carrier, R. L. Synergic effects of crypt-like topography and ECM proteins on intestinal cell behavior in collagen based membranes. *Biomaterials* **31**, 7586-7598 (2010). https://doi.org:https://doi.org/10.1016/j.biomaterials.2010.06.036

32 Wang, L., Murthy, S. K., Fowle, W. H., Barabino, G. A. & Carrier, R. L. Influence of micro-well biomimetic topography on intestinal epithelial Caco-2 cell phenotype. *Biomaterials* **30**, 6825-6834 (2009). https://doi.org:https://doi.org/10.1016/j.biomaterials.2009.08.046

33 Creff, J. *et al.* Fabrication of 3D scaffolds reproducing intestinal epithelium topography by high-resolution 3D stereolithography. *Biomaterials* **221** (2019). https://doi.org:https://doi.org/10.1016/j.biomaterials.2019.119404

34 Castaño, A. G. *et al.* Dynamic photopolymerization produces complex microstructures on hydrogels in a moldless approach to generate a 3D intestinal tissue model. *Biofabrication* **11** (2019). https://doi.org:10.1088/1758-5090/ab0478

35 Tai, W., Chen, Z. & Cheng, K. Expression Profile and Functional Activity of Peptide Transporters in Prostate Cancer Cells. *ACS Molecular Pharmaceutics* **10**, 477-487 (2013). https://doi.org:10.1021/mp300364k

36 Holeček, M. Histidine in Health and Disease: Metabolism, Physiological Importance, and Use as a Supplement. *Nutrients* **12** (2020). https://doi.org:10.3390/nu12030848

37 Eibl, R. *et al.* Cellular Agriculture: Opportunities and Challenges. *Annual Review of Food Science and Technology* **12**, 51-73 (2021). https://doi.org:10.1146/annurev-food-063020-123940

38 Richmond, C. A. & Breault, D. T. Move Over Caco-2 Cells: Human-Induced Organoids Meet Gut-on-a-Chip. *Cellular and Molecular Gastroenterology and Hepatology* **5**, 634-635 (2018). https://doi.org:10.1016/j.jcmgh.2018.01.016